

Landslides (2022) 19:2925–2949  
 DOI 10.1007/s10346-022-01952-1  
 Received: 12 December 2021  
 Accepted: 29 July 2022  
 Published online: 6 August 2022  
 © Springer-Verlag GmbH Germany,  
 part of Springer Nature 2022

Shengyao Mei · Shengshui Chen · Qiming Zhong  · Yibo Shan

## Detailed numerical modeling for breach hydrograph and morphology evolution during landslide dam breaching



**Abstract** Landslide dams are common geological disasters in mountainous areas and can pose severe threats to the lives and property of downstream people. In this study, a three-dimensional numerical simulation method was developed to calculate the breaching behaviors and morphological evolution of landslide dams under complex terrain. An explicit finite volume method (FVM) was adopted by solving the Reynolds-averaged Navier–Stokes (RANS) equations and equilibrium suspended and bed load transport equations. The renormalization group (RNG)  $k$ - $\epsilon$  turbulence model and volume of fluid (VOF) method were combined to describe the hydraulic features of the dam-break flow. The collapse mechanism of breach side slope sliding was considered during the landslide dam breaching. The model was verified by a benchmark experiment case and then applied to study the breach mechanisms and process of the “11.03” Baige landslide dam. Herein, the actual topography of the Baige landslide dam was reconstructed using rapid spatial information processing technology. The comparison showed that the calculated breach hydrograph was consistent with the measured data. Also, the calculated free surface elevation, flow depth, and average flow velocity at each key monitoring point contributed to the mutual corroboration of the breach mechanisms in the field measurements and numerical modeling. Furthermore, the calculated breach morphologies were in accordance with the measured actual topographies at different cross-sections along the Baige landslide dam. After comparing with the typical landslide dam breach models, the model performance showed that the numerical simulation method in this study enhanced the understanding of the dynamic process during landslide dam breaching.

**Keywords** Landslide dam · Breach mechanisms · Numerical simulation · Breach hydrograph · Breach morphology

### Introduction

Landslide dams are common in mountainous regions and are usually triggered by natural hazards such as rainfall and earthquakes (Costa and Schuster 1988; Fan et al. 2020; Shen et al. 2020a; Zhong et al. 2021). Due to a lack of drainage facilities, most landslide dams breach shortly after their formation. Historically, about 85% of landslide dams lasted for less than 1 year, and about 30% lasted for less than 1 day (Costa and Schuster 1988; Peng and Zhang 2012; Shen et al. 2020a). In addition, over 90% of the documented landslide dam failures were overtopping-induced (Costa and Schuster 1988; Zhang et al. 2016; Zhong et al. 2021). Outburst floods due to landslide dam breaching may pose a serious threat to nearby life and property as well as cause serious damage to the ecological

environment and infrastructure within the inundation area. For instance, on April 9, 2000, in China, a huge rockslide occurred due to warming temperatures and snow melt, which completely blocked the Yigong Zangpo River. On June 10, 2000, the landslide dam failed due to overtopping, with a peak breach flow discharge of 94,013 m<sup>3</sup>/s, resulting in hundreds of deaths and leaving millions of people homeless (Zhou et al. 2016). On May 12, 2008, rockslides and rock avalanches triggered by the Wenchuan earthquake produced 257 landslide dams distributed along the fault rupture zone and river channels (Cui et al. 2009); among them, the Tangjiashan landslide dam had the greatest water storage capacity of  $3.16 \times 10^8$  m<sup>3</sup> and posed the most severe threat (Liu et al. 2010). Due to manual intervention, the landslide dam was breached on June 10, 2008, with a peak discharge of 6500 m<sup>3</sup>/s and over 250,000 people in the downstream risk area were evacuated (Chen et al. 2015a). On October 10 and November 3, 2018, two successive rockslides dammed the Jinsha River at the same position near Baige Village, Tibet, China, causing the evacuation of tens of thousands of people and enormous economic losses (Fan et al. 2019; Zhong et al. 2020a). Accurate prediction of the overtopping-induced landslide dam breach process is of great importance for creating effective emergency response contingencies.

In recent years, numerous studies have investigated the breach mechanisms and processes of landslide dams due to overtopping failure. Physical model tests are the primary research method and can be categorized as small-scale flume model tests (with the dam height less than 1 m) (Zhou et al. 2019; Zhu et al. 2021), large-scale field model tests (with the dam height ranging from 1 m to several meters) (Zhang et al. 2021; Takayama et al. 2021), centrifugal model tests (Zhao et al. 2019), and in situ tests (Liu et al. 2010; Cai et al. 2020). Although different classifications are used in the existing literature, the landslide dam breach process can be divided into three stages, including the initial stage, acceleration stage, and stable stage. Furthermore, the variations of influencing factors on the breach process have also been studied. The major influencing factors include landslide dam morphology (i.e., dam height (Walder et al. 2015), slope ratio (Gregoretti et al. 2010)), physical and mechanical properties of landslide dam deposits (i.e., grain-size distribution (Zhu et al. 2020), initial water content (Jiang and Wu 2020), soil density (Chen et al. 2015b)), hydrodynamic conditions of the dammed lake (i.e., river channel slope ratio (Jiang and Wei 2020), upstream inflow (Zhou et al. 2019), surge wave (Peng et al. 2021)), and initial breach size (Zhao et al. 2018). Analyzing the factors influencing the evolution of breach morphology and the associated hydrograph can provide beneficial knowledge regarding the breach mechanisms of a landslide dam due to overtopping.

Numerous numerical models have been developed in recent decades to simulate the overtopping-induced breach process of landslide dams. Similar to embankment dams (ASCE/EWRI Task Committee on Dam/Levee Breaching 2011; Zhong et al. 2016), landslide dam breach models can be classified as parametric, simplified physically based, or detailed physically based. Based on the documented breach information of landslide dams, the regression method is commonly used to develop empirical formulas for calculating breaching parameters in parametric models, which can efficiently simulate peak breach flow (Costa 1985; Evans 1986; Costa and Schuster 1988; Walder and O'Connor 1997; Peng and Zhang 2012; Shan et al. 2022), final breach size (Peng and Zhang 2012), and failure time (Peng and Zhang 2012). Because the parametric models can not consider dam breach processes, the simplified physically based models are attractive for engineering applications (ASCE/EWRI Task Committee 2011; Wu 2013). However, breach models for embankment dams were utilized in the past to model landslide dam breaching. In recent years, a series of simplified physically based models have been proposed, especially for landslide dams, such as DABA (Chang and Zhang 2010; Peng et al. 2014; Shi et al. 2015; Zhang et al. 2019; Chen et al. 2020a), DB-IWHR (Chen et al. 2015a, 2018, 2020b; Wang et al. 2016; Cai et al. 2020), and DB-NHRI (Zhong et al. 2018; Zhong et al. 2020a, b; Shen et al. 2020b; Mei et al. 2021; Yang et al. 2021). In this type of numerical model, the broad-crested weir formula was commonly used to simulate the breach flow discharge under the assumption that the breach cross-section was an inverted trapezoid, while the erosion rate formulas and the limit equilibrium method were utilized to model the continuous erosion of dam materials and intermittent instability of breach side slopes, respectively. Although the simplified physically based landslide dam breach models are computationally efficient and consider the necessary physical processes, they also have shortcomings due to the simplifications and assumptions made regarding the hydrodynamic and morphological processes.

With the development of sediment science and computational fluid dynamics (CFD), one-, two-, and three-dimensional numerical models have been developed to simulate the dam breaching processes. These models are based on hydrodynamic and sediment transport equations and assume shallow water conditions and hydrostatic pressure distribution. This type of model primarily includes three modules: a hydrodynamic module (i.e., continuity and momentum conservation equations of clean or muddy water), a sediment transport module (i.e., equilibrium or nonequilibrium sediment transport equations), and a morphological evolution module (i.e., bed erosion equations and slope instability equations). Based on the types of sediment transport equations used in the numerical model, the detailed physically based dam breach models can be classified as capacity models, non-capacity models, two-phase flow models, and two-layer transport models (Guan et al. 2014).

In general, numerical modeling on landslide dam breaching is in the primary stage. There is no scientific consensus on the evolution of the landslide dam breach process, especially in the longitudinal section (Zhong et al. 2018, 2020b). Although acceptable simulation results can be efficiently provided by the parametric and simplified physically based models, they cannot describe the actual landslide dam breach process. Most of the detailed physical models focused

on embankment or landslide dams are one or two dimensional, but few works were available on three-dimensional models for this topic (Marsooli and Wu 2015; Issakhov and Zhandaulet 2020). Thus, an applicable three-dimensional model that can describe the actual breach hydrograph and morphology evolution during landslide dam breaching is sorely needed.

In this study, a three-dimensional numerical simulation method was developed to calculate the landslide dam breach process. The RANS equations were adopted to depict the hydrodynamic characteristics of breach flow. To close the RANS equations, the RNG *k-ε* turbulence model was used. The equilibrium sediment transport equations for bedload and suspended load was utilized to simulate soil erosion during dam breaching. The collapse of the breach side slope was also taken into account. The model was validated by a benchmark experiment case of dam-break flows; then, the "11.03" Baige landslide dam formed on the Jinsha River in 2018, China, was examined as a case study for numerical simulation considering the actual three-dimensional topography. The reason for the selection of the Baige landslide dam is that the hydrodynamic information regarding variations in breach flow discharge and water level in the dammed lake, as well as the morphological information of the cross-sections in breach channel after dam breaching, were documented in detail. The accuracy of the numerical model was verified by comparing the measured and calculated breach hydrographs and final breach morphologies.

## Numerical modeling of the landslide dam breach process

The complex topography of the landslide dam tends to significantly increase the amount of calculation required in the numerical model. Therefore, a detailed, physically based hydrodynamic model is used to predict the landslide dam breach process. The numerical model consists of three modules, i.e., the hydrodynamic module, sediment transport module, and morphology evolution module. The technical details of the model are described as follows.

### Hydrodynamic module

Based on the Cartesian coordinate system, the RANS equations is utilized to describe the three-dimensional incompressible fluid motion, and the continuity equation is (Duan et al. 2012)

$$\frac{\partial \rho_w}{\partial t} V_F + \frac{\partial}{\partial t} \rho_w u A_x + \frac{\partial}{\partial t} \rho_w v A_y + \frac{\partial}{\partial t} \rho_w w A_z = 0 \quad (1)$$

where  $\rho_w$  = water density;  $t$  = time;  $V_F$  = ratio of the water passing through an element to total volume of the element;  $u$ ,  $v$ , and  $w$  = flow velocity in the  $x$ -,  $y$ -, and  $z$ -directions, respectively;  $A_x$ ,  $A_y$ , and  $A_z$  = flow passing areas in the  $x$ -,  $y$ -, and  $z$ -directions, respectively.

According to continuum mechanics, the momentum equations can be expressed as (Duan et al. 2012; Movahedi et al. 2018)

$$\begin{cases} \frac{\partial u}{\partial t} + \frac{1}{V_F} (u A_x \frac{\partial u}{\partial x} + v A_y \frac{\partial u}{\partial y} + w A_z \frac{\partial u}{\partial z}) = -\frac{1}{\rho_w} \frac{\partial P}{\partial x} + G_x + f_x \\ \frac{\partial v}{\partial t} + \frac{1}{V_F} (u A_x \frac{\partial v}{\partial x} + v A_y \frac{\partial v}{\partial y} + w A_z \frac{\partial v}{\partial z}) = -\frac{1}{\rho_w} \frac{\partial P}{\partial y} + G_y + f_y \\ \frac{\partial w}{\partial t} + \frac{1}{V_F} (u A_x \frac{\partial w}{\partial x} + v A_y \frac{\partial w}{\partial y} + w A_z \frac{\partial w}{\partial z}) = -\frac{1}{\rho_w} \frac{\partial P}{\partial z} + G_z + f_z \end{cases} \quad (2)$$

where  $P$  = intensity of pressure;  $G_x, G_y,$  and  $G_z$  = mass acceleration in the  $x$ -,  $y$ -, and  $z$ -directions, respectively;  $f_x, f_y,$  and  $f_z$  = terms of viscous acceleration in the  $x$ -,  $y$ -, and  $z$ -directions, respectively.

When a breach flood spreads on the downstream slope of a landslide dam, the water surface changes violently, resulting in complex flow patterns. In order to improve computational efficiency, the RNG  $k$ - $\epsilon$  turbulence model is used to model the nonlinear Reynolds stress term. The governing equations for the RNG  $k$ - $\epsilon$  turbulence model are (Yakhot et al. 1992)

$$\frac{\partial(\rho_w k)}{\partial t} + \frac{\partial(\rho_w k u_i)}{\partial x_i} = \frac{\partial}{\partial x_j} \left[ \left( \mu + \frac{\mu_t}{\sigma_k} \right) \frac{\partial k}{\partial x_j} \right] + G_k - \rho_w \epsilon \quad (3)$$

$$\frac{\partial(\rho_w \epsilon)}{\partial t} + \frac{\partial(\rho_w \epsilon u_i)}{\partial x_i} = \frac{\partial}{\partial x_j} \left[ \left( \mu + \frac{\mu_t}{\sigma_\epsilon} \right) \frac{\partial \epsilon}{\partial x_j} \right] + C_1 G_k \frac{\epsilon}{k} - C_2 \rho_w \frac{\epsilon^2}{k} \quad (4)$$

where  $k$  = turbulent kinetic energy;  $\epsilon$  = turbulence dissipation rate;  $u_i$  = flow velocity vector in different directions,  $i$  can be  $x$ -,  $y$ -, or  $z$ -direction;  $\mu$  = turbulent viscosity coefficient;  $\mu_t$  = dynamic turbulence viscosity,  $\mu_t = C_\mu k^2 / \epsilon$ , in which,  $C_\mu = 0.085$ ;  $G_k$  = generation of turbulent kinetic energy from the velocity gradients;  $C_1 = 1.42$ ,  $C_2 = 1.68$ ,  $\sigma_k = \sigma_\epsilon = 0.7194$ .

### Sediment transport module

During the landslide dam breach process, the sediment movement modes can be converted between bedload and suspended load (Cui et al. 2013; Guan et al. 2014). Variations in sediment concentration in the flow discharge can result in variations in flow density and viscosity coefficient, thereby affecting the subsequent erosion. Suspended sediments commonly have low concentration and can be transported by fluid flow. However, bedload sediments are not easily displaced due to limitations imposed by adjacent particles. Herein, a packed bed term is introduced, which denotes an erodible solid component defined by the maximum packing fraction. The surface of packed sediment particles can be moved in the form of bedload transport through rolling, saltating, sliding, or drawing along the bed (Samma et al. 2020). The suspended load can be converted into bedload when deposition velocity exceeds the bed erosion velocity.

In the sediment transport simulation, calculating the hydrodynamic force around a single sediment particle and the boundary layer at the interface is difficult. Therefore, empirical models were commonly used due to the complexity of the sediment transport process. Entrainment and deposition can be regarded as two opposite micro-processes that commonly occur simultaneously. They are combined to obtain the net exchange rate between packed and suspended sediments. As for entrainment, Eq. (5) can be used to calculate the amount of packed sediment converted to suspension (Mastbergen and Berg 2010).

$$E = \alpha_i n_s d_*^{0.3} (\theta_i - \theta_{cr,i})^{1.5} \left[ g \left( \frac{\rho_s - \rho_w}{\rho_w} \right) d_i \right]^{0.5} \quad (5)$$

where  $E$  = upward entrainment velocity;  $\alpha_i$  = entrainment rate coefficient for sediment species  $i$ ;  $n_s$  = normal direction vector

for packed bed interface;  $d_*$  = dimensionless grain size parameter,  $d_* = d_i [\rho_w (\rho_s - \rho_w) g / \mu^2]^{1/3}$ , in which,  $d_i$  = diameter for sediment species  $i$ ,  $\rho_s$  = density of the sediment material;  $\theta_i$  = local Shields parameter,  $\theta_i = \tau / [g d_{50} (\rho_s - \rho_w)]$ , in which,  $\tau$  = local bed shear stress,  $d_{50}$  = mean grain diameter;  $\theta_{cr,i}$  = dimensionless critical Shields parameter,  $\theta_{cr,i} = 0.3 / (1 + 1.2 d_*) + 0.055 [1 - e^{(-0.02 d_*^*)}]$  (Soulsby 1997).

Breach morphology evolution is also affected by the repose angle that accounts for the slope stability supported by the packed sediment, i.e., packed sediment with a small repose angle is prone to instability. Therefore, the modified dimensionless critical Shields parameter can be expressed as (Soulsby 1997)

$$\theta_{cr,i}' = \theta_{cr,i} \frac{\cos \psi \sin \beta + \sqrt{\cos^2 \beta \tan^2 \phi_i - \sin^2 \psi \sin^2 \beta}}{\tan \phi_i} \quad (6)$$

where  $\theta_{cr,i}'$  = modified dimensionless critical Shields parameter;  $\beta$  = angle of bed slope;  $\phi_i$  = repose angle of sediment species  $i$ ;  $\psi$  = angle between the flow and upslope direction.

The deposition or packing rate represents sediment particles settling out of suspension onto the packed bed or resting in bedload transport due to their weight, which can be defined as the product of the effective settling velocity and suspended sediment concentration in the near bed.

$$D = \omega_i c_i \quad (7)$$

where  $D$  = downward sediment deposition velocity;  $\omega_i$  = settling velocity for sediment species  $i$ ,  $\omega_i = \nu_f [(10.36^2 + 1.049 d_*^3)^{0.5} - 10.36] / d_i$  (Soulsby 1997), in which,  $\nu_f$  = Kinematic viscosity of fluid;  $c_i$  = near bed suspended sediment concentration of sediment species  $i$ .

Furthermore, numerous empirical or semi-empirical models have been proposed to simulate bedload transport. Most empirical models used the isolated factor method to establish bed load formulas based on numerous experiments (i.e., Meyer-Peter and Muller 1948). Semi-empirical models commonly determine the basic structure of the bedload formulas based on a certain assumption of general physics. Some parameters in the formulas may need to be calibrated using measured data (i.e., Bagnold 1966; Van Rijn 1984; Nielsen 1992). Significant discrepancies tend to exist between these formulas when they are applied in engineering practice. The following representative dimensionless bedload sediment transport rate formula can be obtained by analyzing and summarizing the existing studies (Chien and Wan 1983).

$$\Phi = \begin{cases} K \Theta^x (\Theta - \Theta_c)^y (\sqrt{\Theta} - \lambda \sqrt{\Theta_c})^z & \Theta > \Theta_c \\ 0 & \Theta \leq \Theta_c \end{cases} \quad (8)$$

where  $\Phi$  = dimensionless bedload sediment transport rate,  $\Phi = q_b (\rho_w / (\rho_s - \rho_w) g d_i)^{0.5} / \rho_w g$ ;  $\Theta$  = the other format of the Shields number,  $\Theta_c$  = sediment incipient motion condition,  $\Theta_c = 0.047$ ;  $K$  = bedload coefficient;  $x, y, z,$  and  $\lambda$  = relevant coefficients.

To select the appropriate bedload formula for sediment transport in this study, several representative formulas (i.e., Meyer-Peter and Muller 1948; Bagnold 1966; Engelund and Fredsoe 1976; Van Rijn 1984; Nielsen 1992) are compared with measured data (Table 1). Single-fraction measured data from multiple sources

**Table 1** The dimensionless forms of typical bed-load formulas

Investigators	Equations	Parameters
Meyer-Peter and Muller (1948)	$\Phi = K(\Theta - \Theta_c)^{1.5}$	$K=8, \Theta_c=0.047$
Bagnold (1966)	$\Phi = K\Theta(\sqrt{\Theta} - \sqrt{\Theta_c})$	$K=10, \Theta_c=0.047$
Engelund and Fredsoe (1976)	$\Phi = K(\Theta - \Theta_c)(\sqrt{\Theta} - 0.7\sqrt{\Theta_c})$	$K=11.5, \Theta_c=0.047$
Van Rijn (1984)	$\Phi = Kd_i^{-0.3}(\frac{\Theta}{\Theta_c} - 1)^{2.1}$	$K=0.053, \Theta_c=0.031$
Nielsen (1992)	$\Phi = K\Theta^{0.5}(\Theta - \Theta_c)$	$K=12, \Theta_c=0.047$

were selected (Meyer-Peter and Muller 1948; Chien and Wan 1999; Roseberry et al. 2012), covering sediment sizes ranging from 0.785 to 28.65 mm and specific gravities ranging from 1.25 to 4.22 (Fig. 1). The Meyer-Peter and Muller formula seems to have the most accurate predictions in the weak sediment transport stage (flow parameter  $\psi = 1/\Theta > 2$ ); therefore, the Meyer-Peter and Muller formula (Eq. 9) was chosen in this paper to compute the bedload sediment transport considering the broad graded characteristics of landslide dam deposits.

$$q_b = K(\theta_i - \theta_{cr,i})^{1.5} \left[ g \left( \frac{\rho_s - \rho_w}{\rho_w} \right) d_i^3 \right]^{0.5} \quad (9)$$

where  $q_b$  = volumetric bedload transport rate per unit width.

To compute the motion of bedload transport in each computational cell, the bedload layer thickness needs to be estimated (Van Rijn 1984) and  $q_b$  is converted into bedload velocity.

$$\frac{\delta_b}{d_i} = 0.3d_i^{0.7} \left( \frac{\theta_i}{\theta_{cr,i}} - 1 \right)^{0.5} \quad (10)$$

$$u_{bedload,i} = \frac{q_b}{\delta_b c_{b,i} f_b} \quad (11)$$

where  $\delta_b$  = bedload layer thickness;  $u_{bedload,i}$  = bedload velocity for sediment species  $i$ ;  $c_{b,i}$  = volume fraction of species  $i$ ;  $f_b$  = critical packing fraction of sediment. The bedload velocity is assumed to

be in the same direction as the fluid flow adjacent to the packed bed interface.

For each sediment species, the suspended sediment concentration can be calculated using the advection-diffusion equation (Samma et al. 2020).

$$\frac{\partial C_{s,i}}{\partial t} + \nabla \cdot (u_{s,i} C_{s,i}) = \nabla \cdot (\xi C_{s,i}) \quad (12)$$

where  $C_{s,i}$  = suspended sediment mass concentration of species  $i$ , which is defined as the sediment mass per volume of the fluid-sediment mixture;  $\xi$  = direction diffusion coefficient;  $u_{s,i}$  = suspended sediment velocity,  $u_{s,i} = u_m + \omega_i c_{s,i}$  in which,  $u_m$  = velocity of the fluid-sediment mixture;  $c_{s,i}$  = suspended sediment volume concentration,  $c_{s,i} = C_{s,i}/\rho_i$ .

**Breach morphology evolution module**

The schematic diagram demonstrating the morphological evolution in the sediment transport model is illustrated in Fig. 2. The morphological evolution in the packed bed can be updated based on the calculation of the previous two modules. The upward entrainment and downward deposition were computed per grid at each time step by the conservation of sediment mass.

$$\phi \frac{\partial z}{\partial t} = \left( \frac{\partial q_{bx}}{\partial x} + \frac{\partial q_{by}}{\partial y} + D - E \right) \quad (13)$$

where  $z$  = bed elevation;  $\phi$  = maximum packing fraction,  $\phi = 0.64$ .

Furthermore, if the angle of bed slope exceeds the critical angle, the sediment and sliding would occur to form a new bed with a slope equal to the new critical value. The new bed slope angle will be established nearly equal to the angle of repose by lowering the higher elevation cell and raising the lower elevation cell (Guan et al. 2014). The process can be described by Eq. (14).

$$\begin{cases} z'_{i+1} = z_{i+1} - \Delta z \\ z'_i = z_i + \Delta z \end{cases} \quad (14)$$

where  $\Delta z$  = the change in the bed's elevation due to sliding and  $\Delta z = \Delta L(\tan\beta - \tan\phi)/2$ ;  $\Delta L$  is the distance of two adjacent cells.

**Numerical solution method**

The continuity and momentum equations in the hydrodynamic module are solved using an explicit FVM on the structured staggered grids. The flow region is subdivided into a mesh with fixed

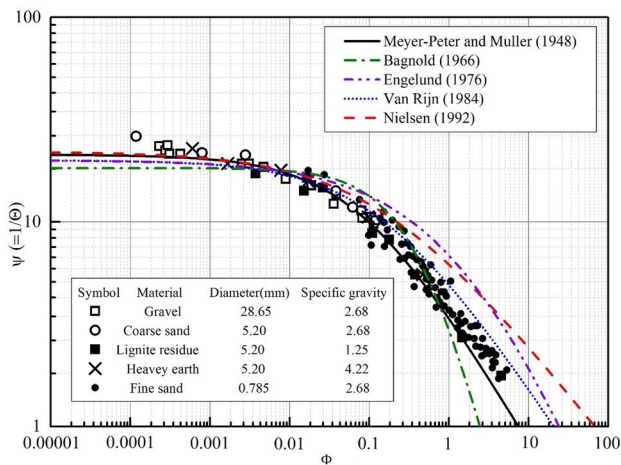
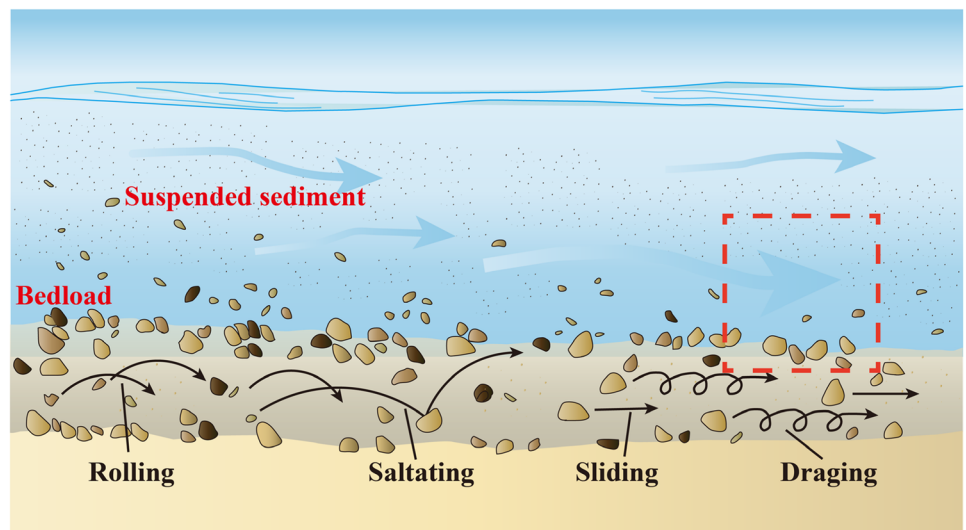
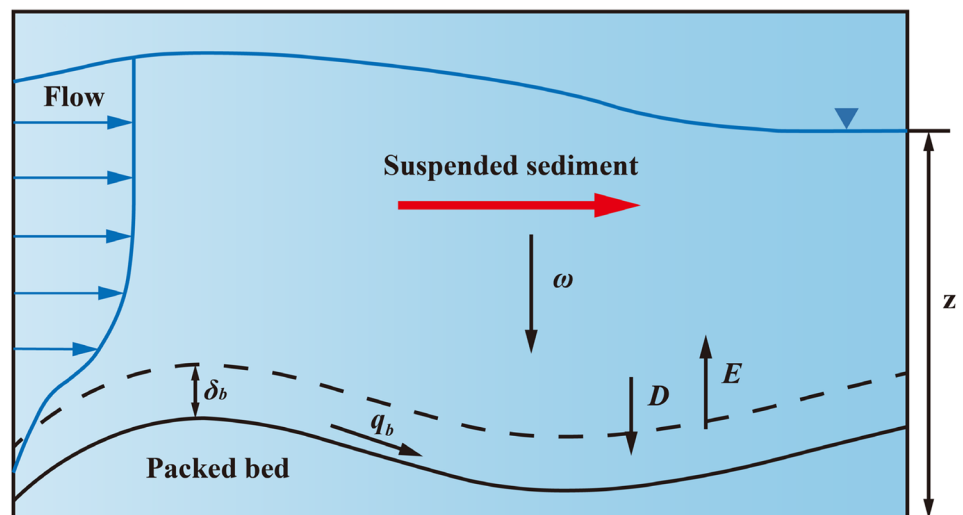


**Fig. 1** Comparison of typical bed-load formulas

**Fig. 2** Schematic representation of sediment transport model. **a** Diagram showing the river load and transportation mechanisms. The red dashed box is shown enlarged in (b); **b** Morphological evolution in a packed bed



**(a)** Diagram showing the river load and transportation mechanisms. The red dashed box is shown enlarged in (b)



**(b)** Morphological evolution in a packed bed

rectangular cells, and there are associated local average values of all dependent variables within each cell. All variables are assumed to be set at the center of each cell except for the flow velocities, which are located at cell faces (staggered grid arrangement). Geometric features of complex solid are embedded in the mesh by defining the fractional face area and fractional volumes of the cells that are open to flow according to the fractional area/volume ratio (FAVOR) method (Liang et al. 2019). The VOF method based on the Euler model (Hirt and Nichols 1981) effectively describes the water–sediment interface, which can track the free-surface flow by the ratio of fluid volume to unit volume.

To construct discrete numerical approximations to the governing equations, control volumes are defined surrounding each dependent variable location. For each control volume, surface fluxes, surface stresses, and body forces can be computed in terms of surrounding variable values. These quantities are then combined

to form approximations for the conservation laws expressed by the equations of motion. Here, the stress in the fluids is assumed to be the sum of a diffusing viscous term and a pressure term, thus describing the viscous flow. The temporal terms are discretized by the Euler scheme, the convection terms are discretized by the exponential scheme, and the diffusion terms are discretized by the central scheme. Moreover, the time-advanced pressures in the momentum equations and time-advanced velocities in the continuity equation are coupled by using the pressure implicit solution based on the pressure-implicit with the splitting of operators (PISO) algorithm (Issakhov and Imanberdiyeva 2019), which is an extension of the semi-implicit method for pressure linked equations (SIMPLE) algorithm used for the solution of incompressible flow problems.

The hydrodynamic and sediment transport modules in the computer code communicate via a time-varying and quasi-steady-state

method. The bed elevation is assumed constant during the flow computation, and the flow and sediment transport quantities are assumed invariant to bed elevation changes during the bed elevation computation. The computation procedure at each time step can be describe as: (I) The dimensionless bed shear stress is calculated at each time step to obtain the equilibrium bedload and related parameters. (II) Calculate the bed elevation change by Eq. (13) according to some empirical functions. (III) Update the volume fraction and flow field as well as the pressure by solving the model system of Eqs. (1)–(4) based on information from the previous steps. (IV) Update the bed elevation at the next time calculated by Eq. (14). (V) Repeat the above procedures until the stopping time is achieved.

### Model validation

In this section, the validation of the present model is tested using a benchmark experiment case carried out at the UCL-Belgium for dam-break flows over mobile beds (Soares-Frazao et al. 2012), which is a representative test case of the recent dam-break models (Marsooli and Wu 2015; Fourtakas and Rogers 2016; He et al. 2017; Rowan and Seaid 2020). As sketched in Fig. 3, the flume had a length and width of 36 and 3.6 m, respectively. The dam break event was simulated by rapidly pulling up a gate with a width of 1 m, which was placed between two impervious blocks 12 m away from the upstream flume end. The rigid bed of the flume was pre-laid with a saturated sand layer with a thickness of 0.085 m, extended from 1 m upstream to 9 m downstream of the gate. The median diameter of the sediment was 1.61 mm, with a density of 2630 kg/m<sup>3</sup> and a porosity of 0.42. The gate center was set as the original coordinate (0, 0). The initial water level of the upstream reservoir was 0.047 m and the downstream reach was dry. The experiment was stopped after 20 s to avoid the reflected wave from the downstream end. The water level was measured at four pairs of gauges located symmetrically downstream of the gate, and the bed elevation was measured along three longitudinal profiles ( $y = 0.2$  m, 0.7 m, and 1.45 m).

In the model, a uniform grid with the size of 0.01 m in each direction was used to cover the entire calculation domain, including the initial sediment bed area and the upstream reservoir. The breach time of numerical simulation was set as 20 s, which was consistent with the test time. Manning roughness ( $n$ ) is set at 0.0165

for the portion covered by the sand layer, and 0.01 for the other portion recommended by International Association for Hydraulic Research (IAHR) (2012). Furthermore, the repose angle of the sediment was 23°.

Due to the symmetric experiment configuration, the calculated and measured water levels from the same pairs of gauges are well coordinated with each other. To verify the proposed numerical model, an indicator, namely mean absolute error (MAE), is introduced to quantify the difference between the calculated and the measured data:

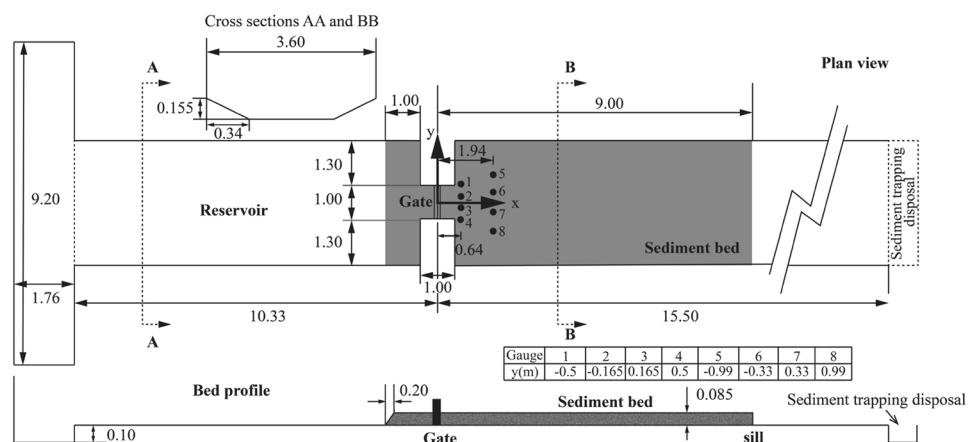
$$\text{MAE}(A) = \frac{\sum_{i=1}^N |A^{m(i)} - A^{c(i)}|}{N} \quad (15)$$

where  $\text{MAE}(A)$  = mean absolute error of the variable  $A$ ;  $i$  = counter of the gauge;  $A^{m(i)}$  = measured data of  $A^{(i)}$ ;  $A^{c(i)}$  = calculated value of  $A^{(i)}$ ;  $N$  = number of the measured data.

The comparison of the calculated and measured variations of the water levels at the four pairs of gauges are shown in Fig. 4. The values of mean absolute errors of the water level at four pairs of gauges are 0.013 m (Fig. 4a), 0.016 m (Fig. 4b), 0.028 m (Fig. 4c), and 0.007 m (Fig. 4d). The water level at the gauges 1–4 show obvious oscillatory behavior, which may due to the rapid changes of bed elevation near the gate. However, a degree of deviations was observed at gauges 5 and 8, where the numerical model underestimated the water levels, mainly due to the errors caused by the departure in the dynamics of the fluid. In general, the performance of the numerical model shows that these quantitative differences are generally reasonable, indicating that the model can well calculate the measured water levels at the four pairs of gauges.

The comparison of the calculated and measured variations of the bed elevation along three longitudinal profiles ( $y = 0.2$  m, 0.7 m, and 1.45 m) are shown in Fig. 5, and the values of mean absolute errors of the bed elevation have the results of 0.018 m (Fig. 5a), 0.015 m (Fig. 5b), and 0.021 m (Fig. 5c). At  $y = 0.2$  and 0.7 m, it is obvious that the erosion occurs near the gate ( $x < 2.0$  m) while deposition occurs at a further distance. However, some discrepancies from the experiment are noticeable, especially around  $x = 2$  to  $x = 4$  m, while the numerical model overpredicts the scouring region. At  $y = 1.45$  m, the agreement marginally deteriorates significantly, with some deviations near the wall at  $x = 0$ –2 m, perhaps due to the adhesion behavior near the wall. In addition, the

**Fig. 3** Schematic of the dam break experiment conducted at UCL-Belgium (dimension in meters) (courtesy of Soares-Frazao et al. 2012)



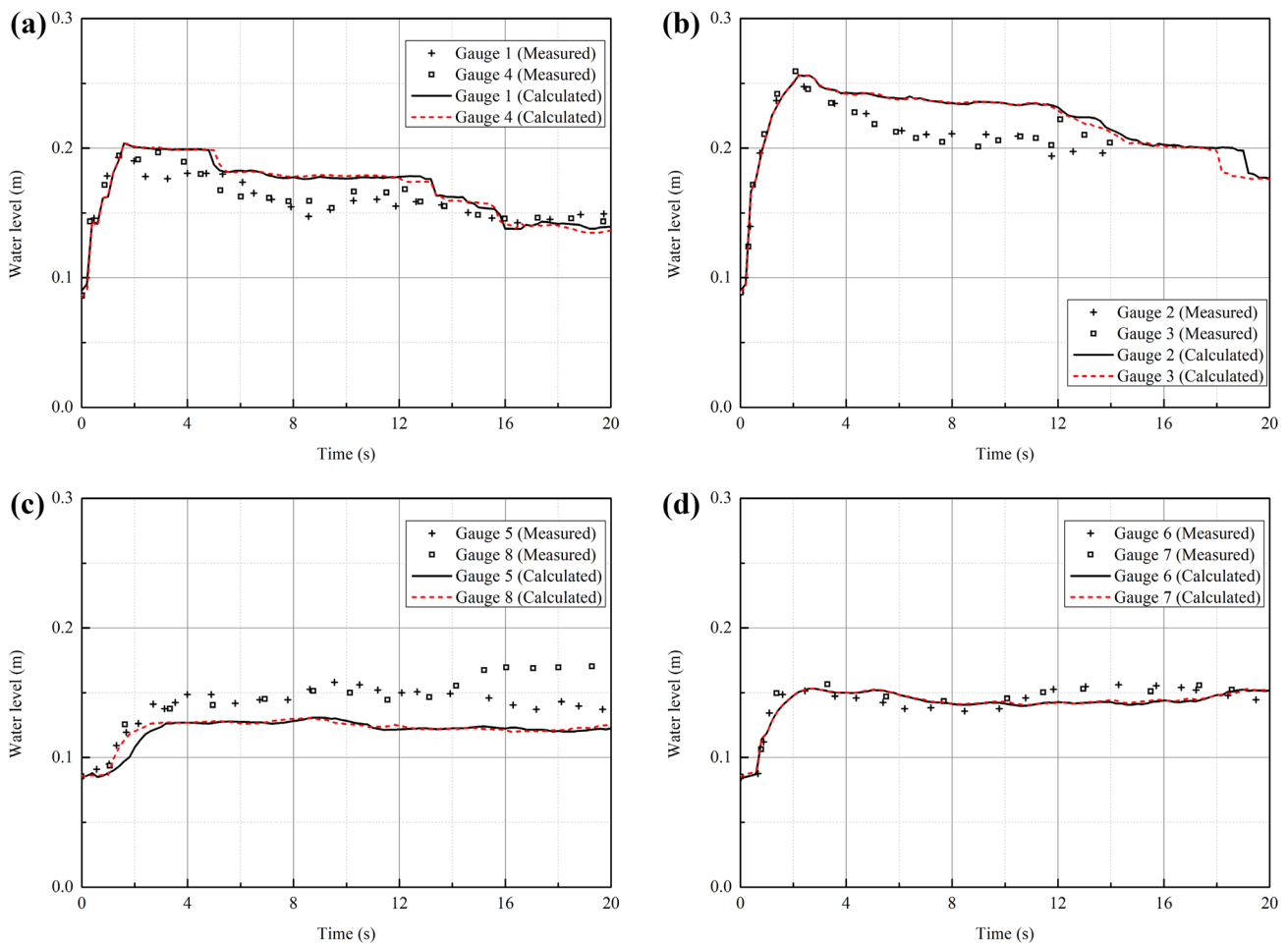


**Fig. 4** Comparison of the calculated and measured variations of the water level at the four pairs of gauges: **a** gauges 1 and 4, **b** gauges 2 and 3, **c** gauges 5 and 8, and **d** gauges 6 and 7

sediment peak is somewhat underpredicted, with a tiny delay in peak position. In general, the reports on the performance of the other numerical models (i.e., Marsooli and Wu 2015; Fourtakas and Rogers 2016; He et al. 2017; Rowan and Seaid 2020) showed that the mean absolute errors of the variations of bed elevation are larger than those of the water level.

Overall, based on the comprehensive comparison of calculated and measured results of the variations of the water level and bed elevation during the erosion process, as well as considering the reports by the other references, the calculated water level at the four pairs of gauges are generally in good agreement with the measurements by Soares-Fraza et al. (2012). In addition, the bed elevations along the three longitudinal profiles satisfactorily reproduced the actual experimental results. Despite certain differences in the comparison, the current model can be utilized to simulate dam-break flows effectively over mobile beds considering the complexity of the three-dimensional dam-break and the challenges brought by fluid dynamics.

#### Case study of the breach process of “11.03” Baige landslide dam

To further demonstrate the performance of the numerical method, the “11.03” Baige landslide dam is examined using detailed measured data as well as to study in detail the evolution of the breach hydrograph and breach morphology.

#### Landslide dam condition

The study area is located at the border between Sichuan Province and Tibet, China (98°42′17.98″E, 31°4′56.41″N) (Fig. 6). At 22:06, on October 10, 2018, the first landslide occurred in this region, completely blocking the main stem of the Jinsha River. From the field investigation (Cai et al. 2020), the “10.10” landslide dam had a volume of approximately 27.5 million m<sup>3</sup> and overtopped naturally without manual intervention two days later. Subsequently, at 17:40 on November 3, 2018, a secondary landslide happened at the same location, forming a high-speed debris flow and blocking the river

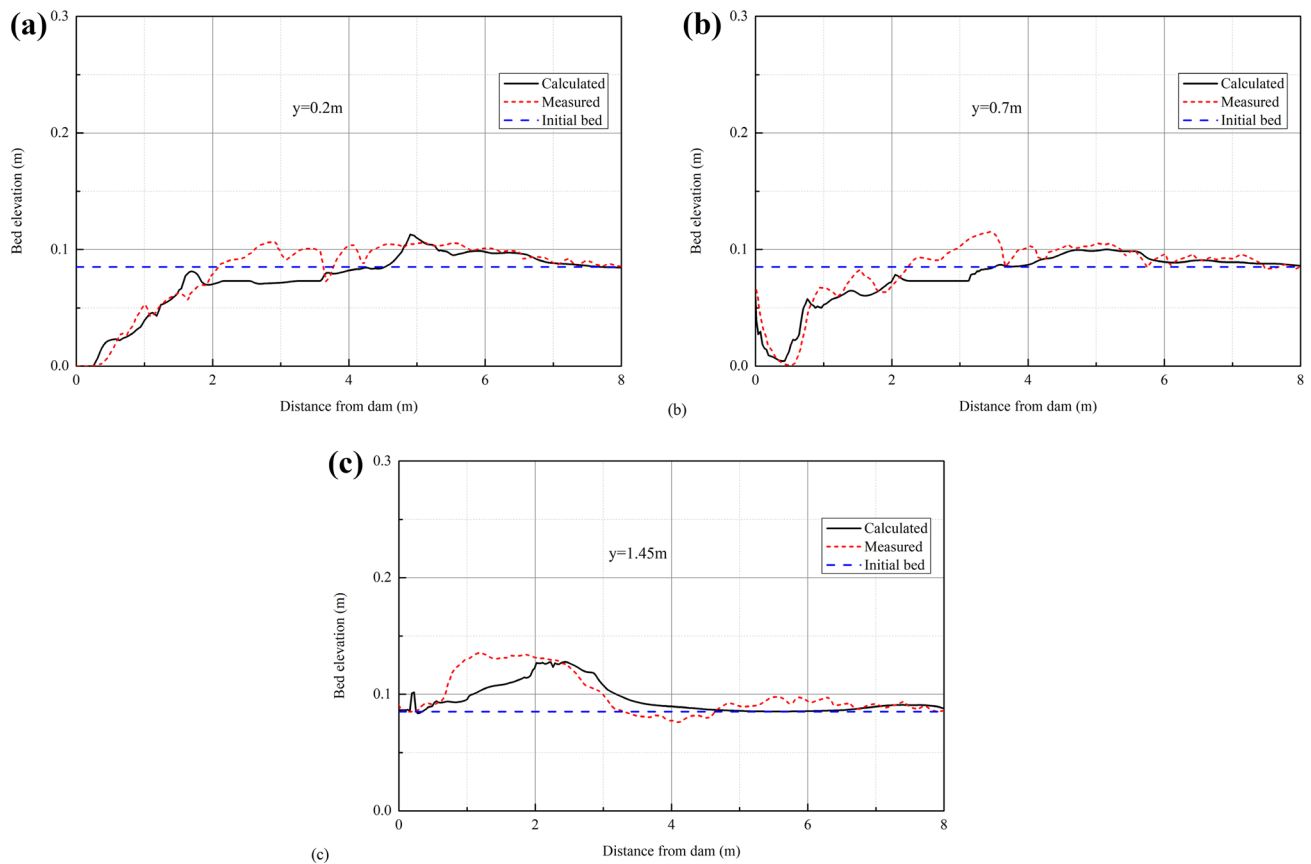


**Fig. 5** Comparison of the calculated and measured variations of the bed elevation along three longitudinal profiles ( $y=0.2\text{ m}$ ,  $0.7\text{ m}$ , and  $1.45\text{ m}$ )

again (Fig. 7). The volume of the second landslide dam was estimated to be approximately 12 million  $\text{m}^3$ . The new landslide dam was observed to pack on top of the earlier residual dam, and the average height of the second landslide dam was 50 m higher than the first one, making the damage caused by the failure of the second landslide dam much worse. Due to the potential large threat and complete monitoring data, this study focuses on the “11.03” landslide dam.

The rapid spatial information processing technology combined with geographic information systems (GIS) and digital elevation model (DEM) altimetry data was used to obtain the morphological characteristics of the landslide deposit (Fig. 8). The elevation of the “11.03” Baige landslide ranged from 3800 m at the mountain to 2870 m at the Jinsha River. The terrain of the landslide accumulation body in the cross and longitudinal sections of the landslide dam is shown in Fig. 9 (Cai et al. 2020). The elevation of the Puerto is 2966 m, and the maximum dam height is approximately 96 m (Zhang et al. 2019; Zhong et al. 2020a). Geological survey data showed that the landslide deposits were primarily composed of gravelly soil, which was generally fine.

After analyzing the dam height, upstream water inflow, and water level rising speed, an artificial spillway was excavated to effectively reduce the stored water in the dammed lake. A spillway was constructed at the Puerto, with a length of 220 m, maximum

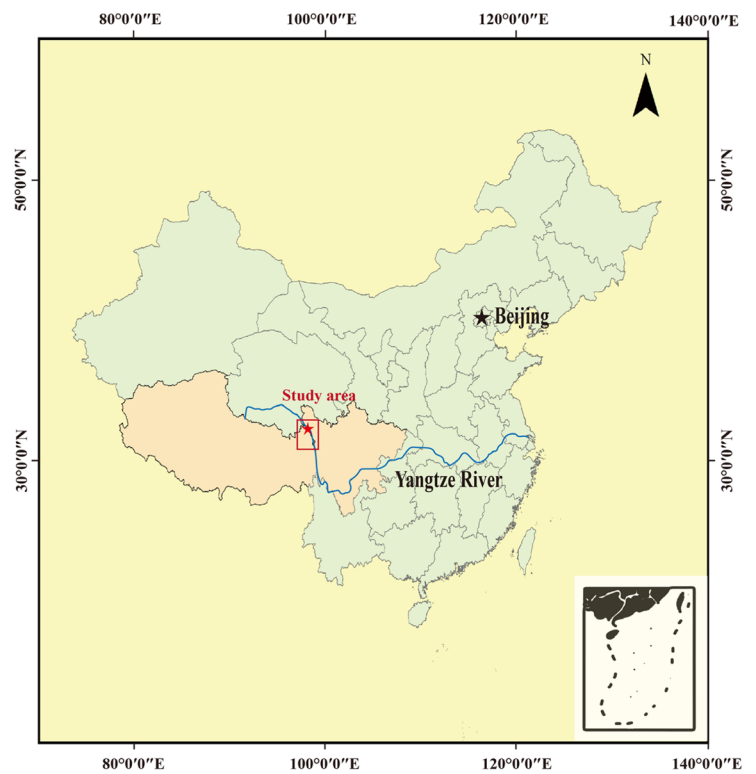
top width of 42 m, a bottom depth of 3 m, and an average depth of 11.5 m. The elevation of the base of the spillway entrance was 2952.5 m. Details of the breach process have been described in multiple studies (i.e., Fan et al. 2019; Zhang et al. 2019; Cai et al. 2020; Zhong et al. 2020a), while this study focuses on water level variations to determine boundary conditions for the numerical model. The upstream water level was 2892.84 m when the landslide dam formed, followed by a rapid increase in water level. At 04:45 a.m. on November 12, the water level rose to 2952.52 m and entered the spillway. At 1:45 p.m. on November 13, the upstream water level reached the maximum value of 2956.4 m, and the water volume in the dammed lake reached 578 million  $\text{m}^3$ . At 6:00 p.m., the peak flow discharge occurred with a value of approximately 31,000  $\text{m}^3/\text{s}$ . At 8:00 p.m. on the same day, the breach flow discharge rapidly attenuated to 7700  $\text{m}^3/\text{s}$ . At 8:00 a.m. the next day, the breach flow discharge was equal to the inflow, and the water level dropped to 2905.75 m, marking the end of the breach process.

### Model set-up

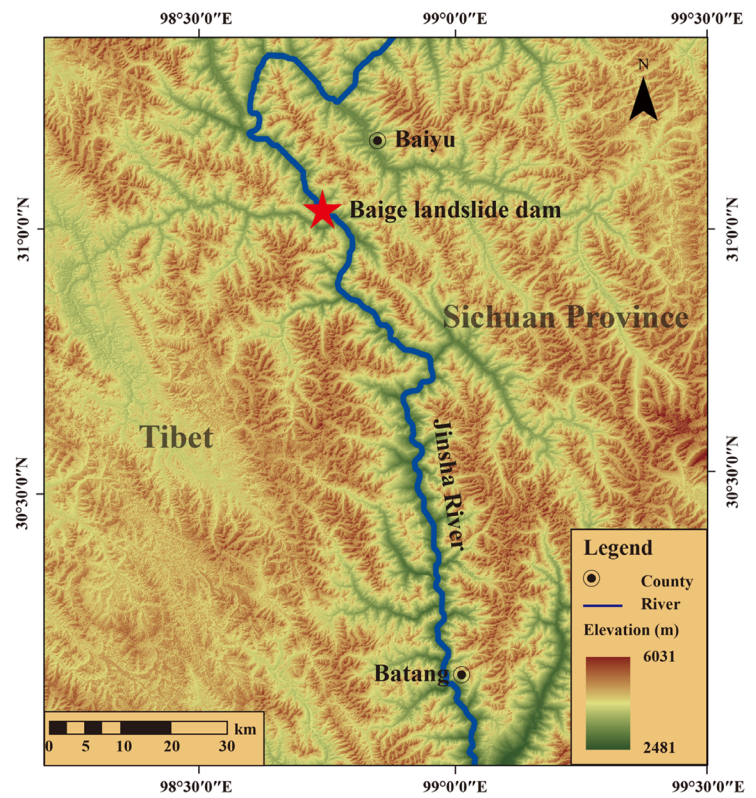
Based on the terrain data before the failure of the “11.03” landslide dam, a three-dimensional solid stereolithography (STL) model was developed. In order to facilitate subsequent grid processing, the solution domain was truncated into a regular rectangular



**Fig. 6** Location of the “11.03” Baige landslide dam. **a** Location map with a red box highlighting the study area; **b** study area with the Baige landslide dam marked by the red star

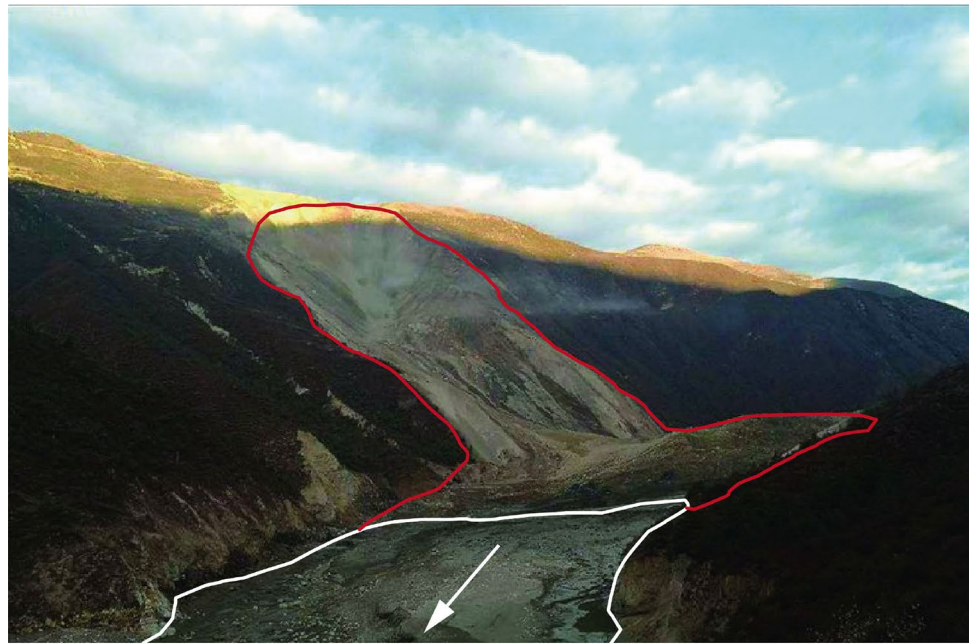


**(a)** Location map with a red box highlighting the study area



**(b)** Study area with the Baige landslide dam marked by the red star

**Fig. 7** Regional photos of the “11.03” Baige landslide dam (photos courtesy of Chinanews.com). **a** Photo of the landslide that occurred on November 3, 2018; **b** Photo of the landslide dam from the upstream view



**(a)** Photo of the landslide that occurred on November 3, 2018



**(b)** Photo of the landslide dam from the upstream view

area  $1150 \text{ m} \times 1050 \text{ m} \times 210 \text{ m}$  (length  $\times$  width  $\times$  height) in size (Fig. 10). A  $4.5 \text{ m} \times 4.5 \text{ m} \times 4.5 \text{ m}$  grid is used for model discretization, and the calculation area has a total of 2.78 million grid elements. The simulation time is set from 04:45 a.m. on November 12 to 10:00 p.m. on November 13. The inflow boundary is upstream of the landslide dam and is set at the specified pressure according to the actual water level, while the top boundary is set at standard atmospheric pressure. The free outflow boundary is downstream of the landslide dam, and the other three boundaries are set as the solid walls. The initial overtopping water level

in Jinsha River was set as 2952.52 m, which was consistent with the elevation at the bottom of the spillway. Table 2 shows the physical and mechanical parameters of sediment material in the numerical simulation. According to the field investigation (Zhang et al. 2019; Cai et al. 2020), the median grain size, sediment density, and angle of repose of the landslide deposit are estimated. Furthermore, the optimum entrainment coefficient and bedload coefficient for dam breach are obtained via sensitivity analysis (Kaurav and Mohapatra 2019). Notably, in the numerical model, four monitoring points are set up to analyze the breach flow

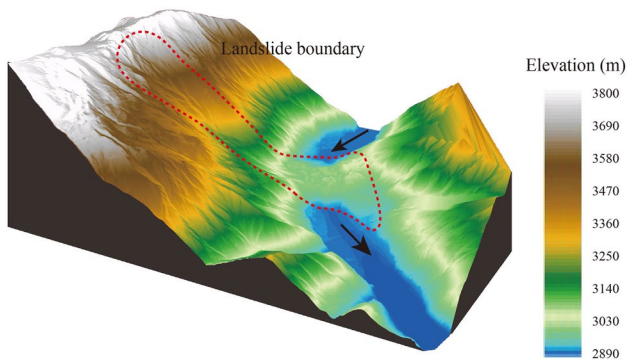


**Fig. 8** Topography of the “11.03” Baige landslide dam

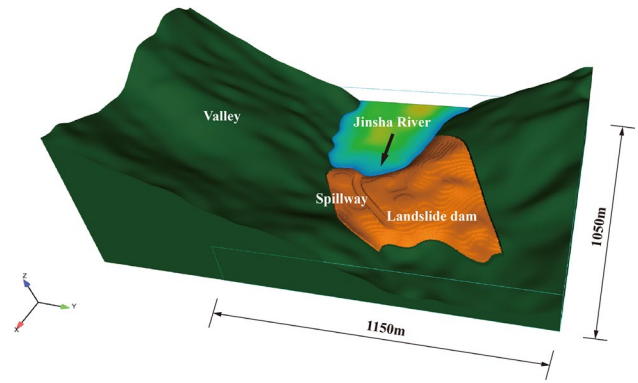
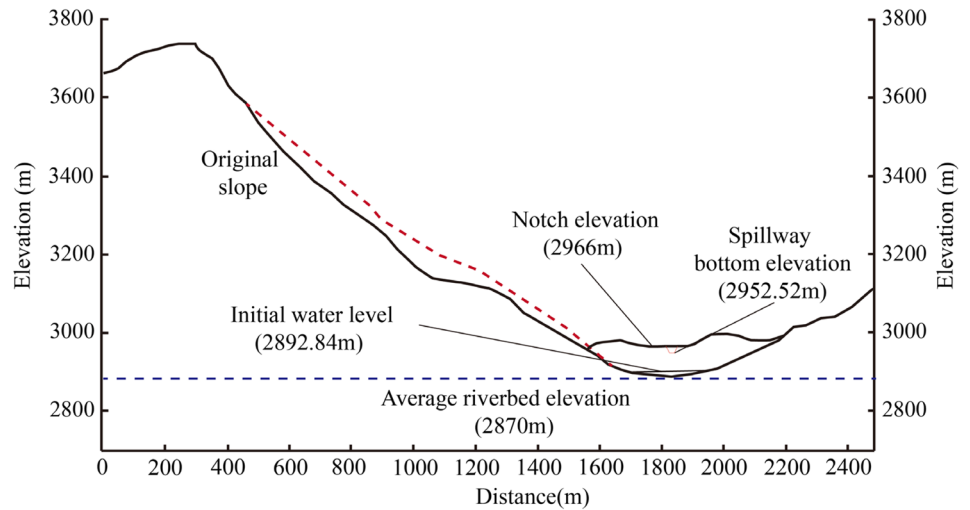


**Fig. 10** Three-dimensional numerical simulation model

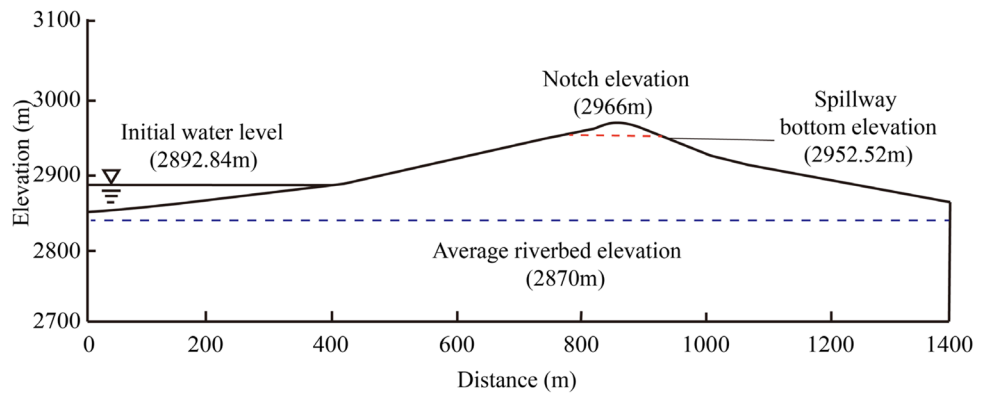
through the landslide dam at different positions (Fig. 11). Points 1 and 2 are placed at the inlet and turning point of the spillway, respectively. Point 3 is placed at the downstream slope of the landslide dam, and point 4 is placed at the downstream toe of

the landslide dam. Furthermore, a flow monitoring section is set to monitor variations in breach flow discharge during the landslide dam breaching process, which is consistent with the in-situ monitoring location.

**Fig. 9** Schematic diagrams of profiles of the “11.03” Baige landslide dam. **a** Cross section; **b** Longitudinal section



**(a)** Cross section



**(b)** Longitudinal section

**Table 2** Sediment particle parameters

Material	$d_{50}$ (mm)	$\rho_s$ (kg/m <sup>3</sup> )	$\alpha$	$K$	$\varphi$ (°)
Sediment	8	2650	0.018	8	38

### Breach process

Unlike embankment dams, landslide dams commonly result from the rapid accumulation of collapsed earth-rock materials without manual compaction (Fan et al. 2020; Zhong et al. 2021). Overtopping failure commonly occurs at the weak intersection of the dam crest and downstream surface, forming the initial breach. As flow increases, the dam breach is continuously undercut and broadened (Fig. 12). Based on observations from the model and in-situ tests, the overtopping failure processes of landslide dams can be classified into the initial, acceleration, and stable stages (Zhang et al. 2019; Zhong et al. 2021). Regarding the variation of breach flow and breach morphology in the cross and longitudinal sections, the landslide dam breach process can be depicted as follows: (1)

Surface and backward erosion. When the water flow overtops the dam crest, numerous small gullies form on the downstream slope toe. Due to the small flow rate in the initial stage, surface erosion dominates. With the continuous rise of the upstream water level in the dammed lake, the gullies on the downstream slope begin to undercut quickly, forming the initial breach. The breach subsequently migrates upstream until it reaches dammed lake. (2) Erosion along the breach channel. When the backward erosion migrates to the dammed lake, the water head above the dam crest increases abruptly, and rapid vertical and lateral erosion occurs on the surface of the breach channel. Also, the flow through the breach channel increases sharply until the peak breach flow is reached. (3) Rebalance of breach channel. Breach expansion leads to a rapid decline in water level in the dammed lake, corresponding to a continuous decrease in breach flow discharge. With the weakening of the hydrodynamic conditions, the evolution of breach morphology attenuates until the water flow is not able to transport the dam deposits, and the suspended load gradually settles downstream of the landslide dam. Finally, the breach process ends when the flow through the breach channel is the same as the upstream inflow.

**Fig. 11** Positions of the monitoring points and flow monitoring section

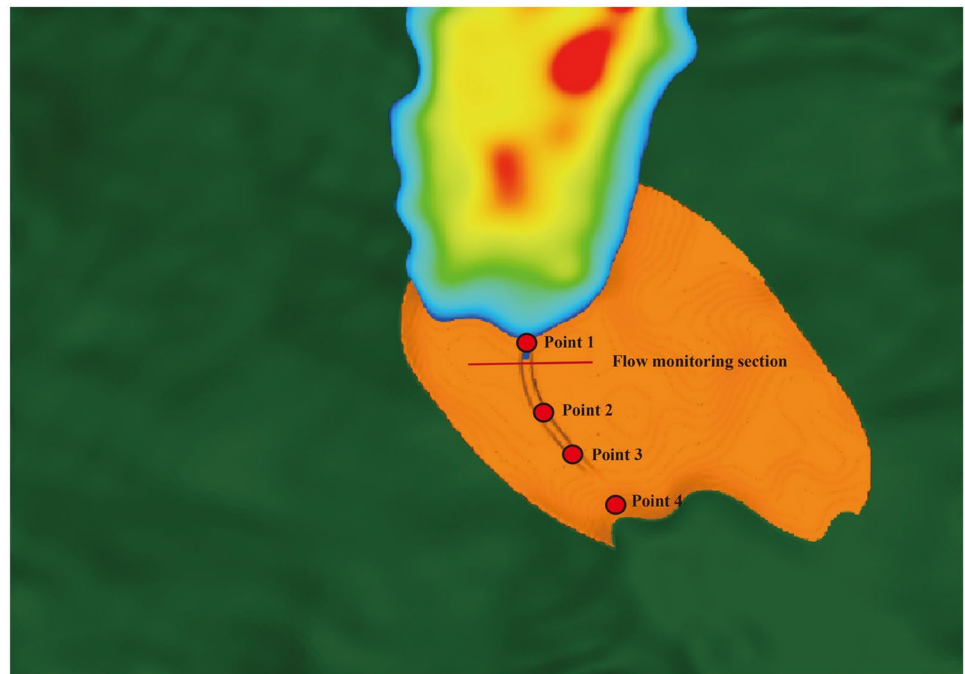


**Fig. 12** Schematic diagram of an overtopping-induced landslide dam breach mechanism. The body of water behind the landslide dam continues to rise until it breaches the top of the natural dam, creating this overtopping-induced landslide dam breach

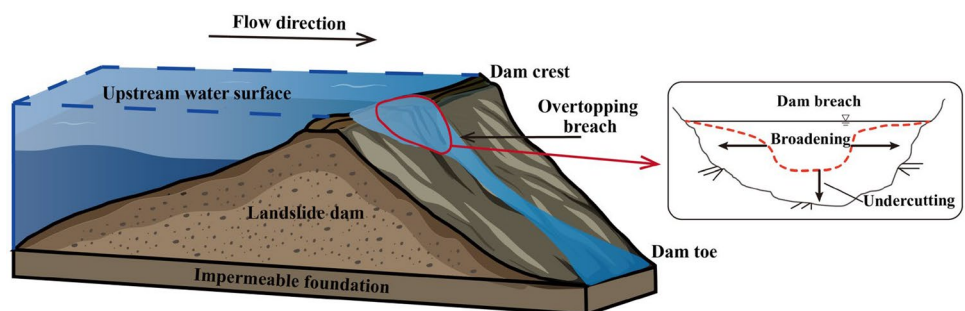
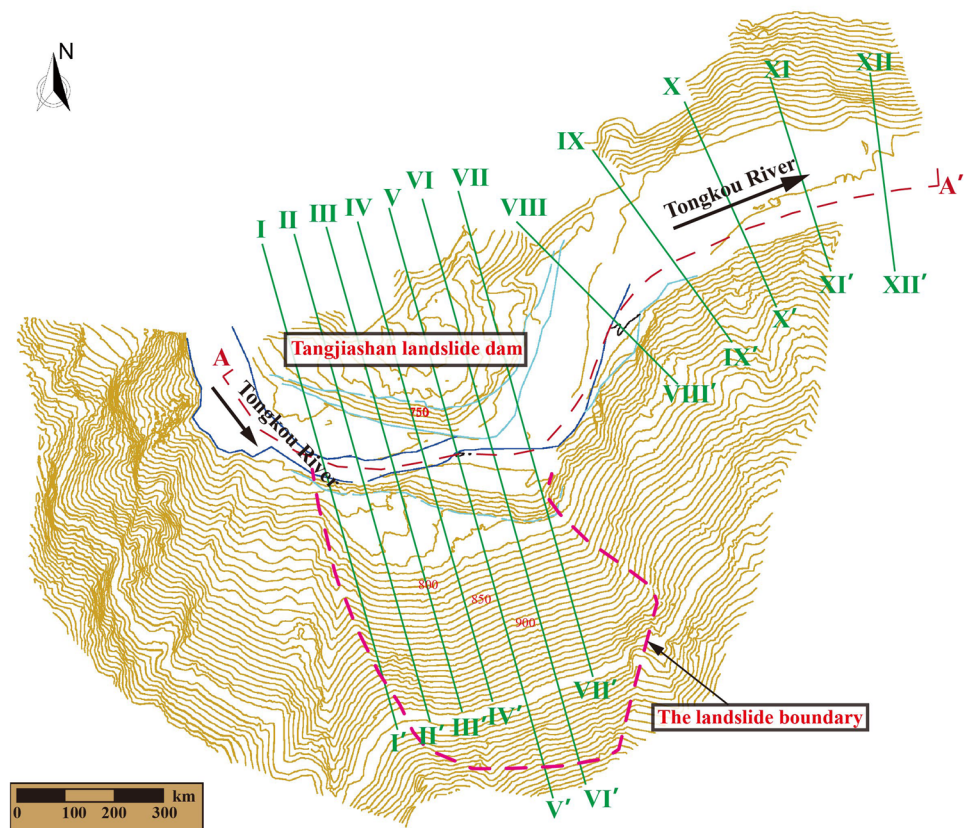
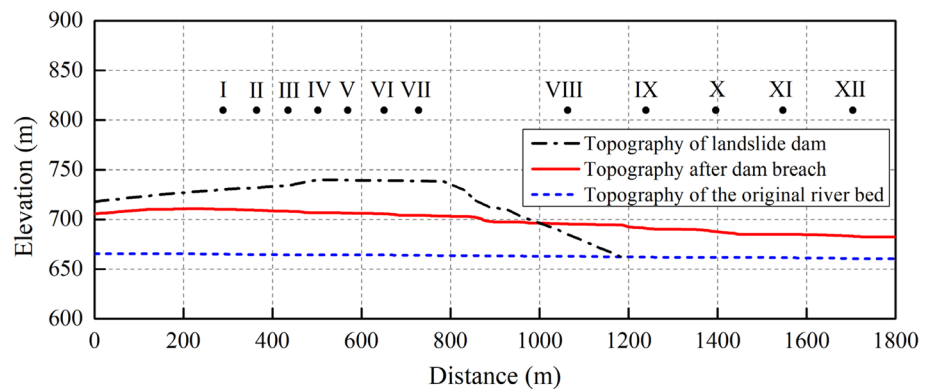


**Fig. 13** Topography of the Tangjiashan landslide dam after breaching. **a** Topographic contour map after the dam breach at Tangjiashan (modified from Liu et al. 2010); **b** Schematic diagram of the topography in the longitudinal cross-section after the dam breach (modified from Liu et al. 2010)



**(a)** Topographic contour map after the dam breach at Tangjiashan (modified from Liu et al., 2010)



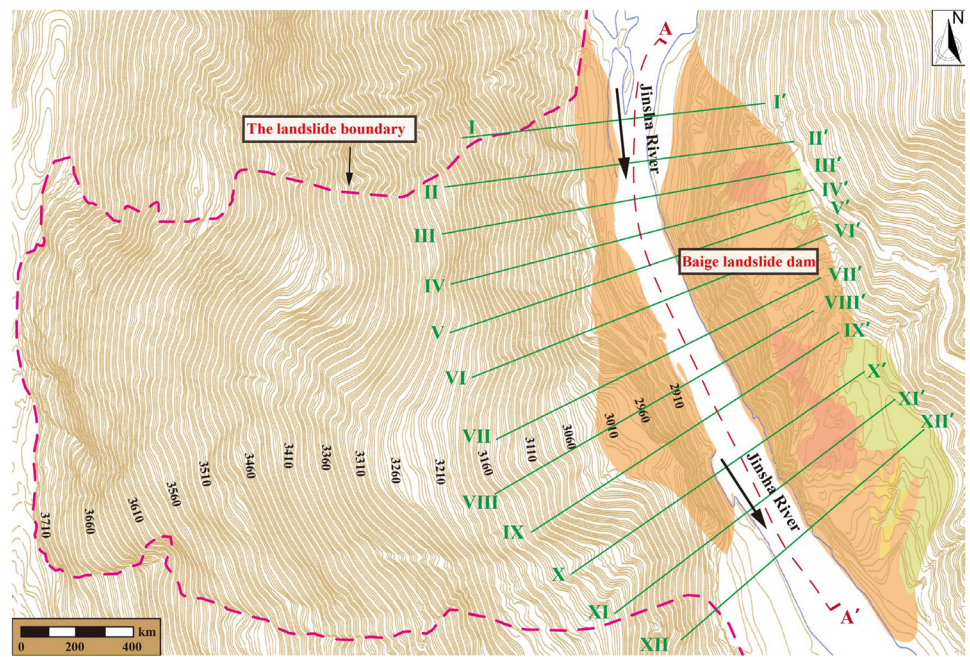
**(b)** Schematic diagram of the topography in the longitudinal cross-section after the dam breach (modified from Liu et al., 2010)

Figures 13 and 14 show the final topography of Tangjiashan and Baige landslide dams after breaching, respectively. The variation of topographies of the two landslide dams demonstrates that, due to incision and deposition effects, the downstream slope ratio in the longitudinal section decreases after dam breaching. Figure 15 shows the simulated results and actual photos of the dynamic breach process at different time. The actual photos and simulated results are similar, and the hydrodynamic and sediment transport processes can be described using the appropriate numerical simulation method.

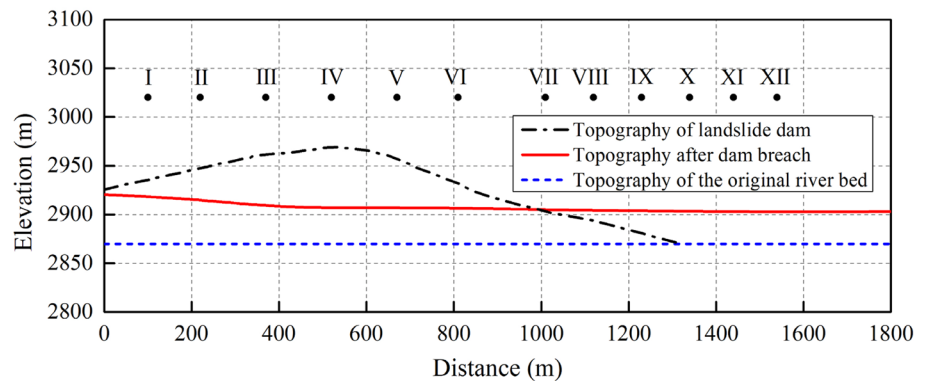
### Breach hydrograph

Figure 16 shows the calculated and breach hydrograph during the “11.03” Baige landslide dam breaching process, which is roughly consistent with the trend of measured data. Table 3 also lists the calculated and measured breaching parameters. The calculated peak breach flow is 29,518 m<sup>3</sup>/s and the relative error with the measured data (31,000 m<sup>3</sup>/s) is reasonable, indicating the validity of the simulated results. Also, the calculated time to the peak is 35.06 h after dam breaching, which is in good agreement with the measured

**Fig. 14** Topography of the Baige landslide dam after breaching. **a** Topographic contour after the dam breach at Baige (modified from Cai et al. 2020); **b** schematic diagram of the topography in the longitudinal cross-section after the dam breach (modified from Cai et al. 2020)



**(a)** Topographic contours after the dam breach at Baige (modified from Cai et al., 2020)



**(b)** Schematic diagram of the topography in the longitudinal cross-section after the dam breach (modified from Cai et al., 2020)

data (37.25 h after dam breaching). Hence, the maximum relative errors for both peak breach flow and time to peak are within  $\pm 10\%$ .

Using the VOF method, the simulation results of the flood propagation and corresponding physical parameters (i.e., free surface elevation, flow depth, and average flow velocity) of the four typical monitoring points during the breach process can be obtained to achieve mutual corroboration between the three-stage breaching process of the landslide dam based on the model tests and numerical simulation. The variations of the three parameters with time at each monitoring point are presented in Figs. 17, 18, and 19, respectively. Due to the weak hydrodynamic conditions at the initial stage of the dam failure, the difference in the values of the monitoring points is slight. The starting time was set at 6:00 p.m. on November 12, 2018. In stage 1, each monitoring point along the flow direction begins to record water flow in sequence with time, and the initial flow depth and average flow velocity maintained a steady low level. Next, the flood runs through the whole spillway,

and the free surface at the entrance (point 1) rose significantly, as did the flow depth. Notably, the average flow velocity at points 3 and 4 increases fastest during this stage, which verified the presence of backward erosion. In particular, the calculated maximum free surface elevation is 2958.6 m, briefly higher than the measured value of 2956.4 m. Later, the free surface elevation at each monitoring point drops rapidly as the breach reached stage 2 and is affected by sustained longitudinal erosion of the spillway. During this stage, the maximum flow depth and average flow velocity at each point were generated, and the breach flow discharge also reached the maximum value. In general, the maximum flow depth at each monitoring point along the flow direction decreased successively. The average flow velocity at Point 1 accelerated significantly due to the sustained downcutting and lateral erosion of the breach. The maximum average flow velocities at the other points were similar to the measured value of 10 m/s (Cai et al. 2020). Subsequently, the free surface elevation entered a stable period, and it

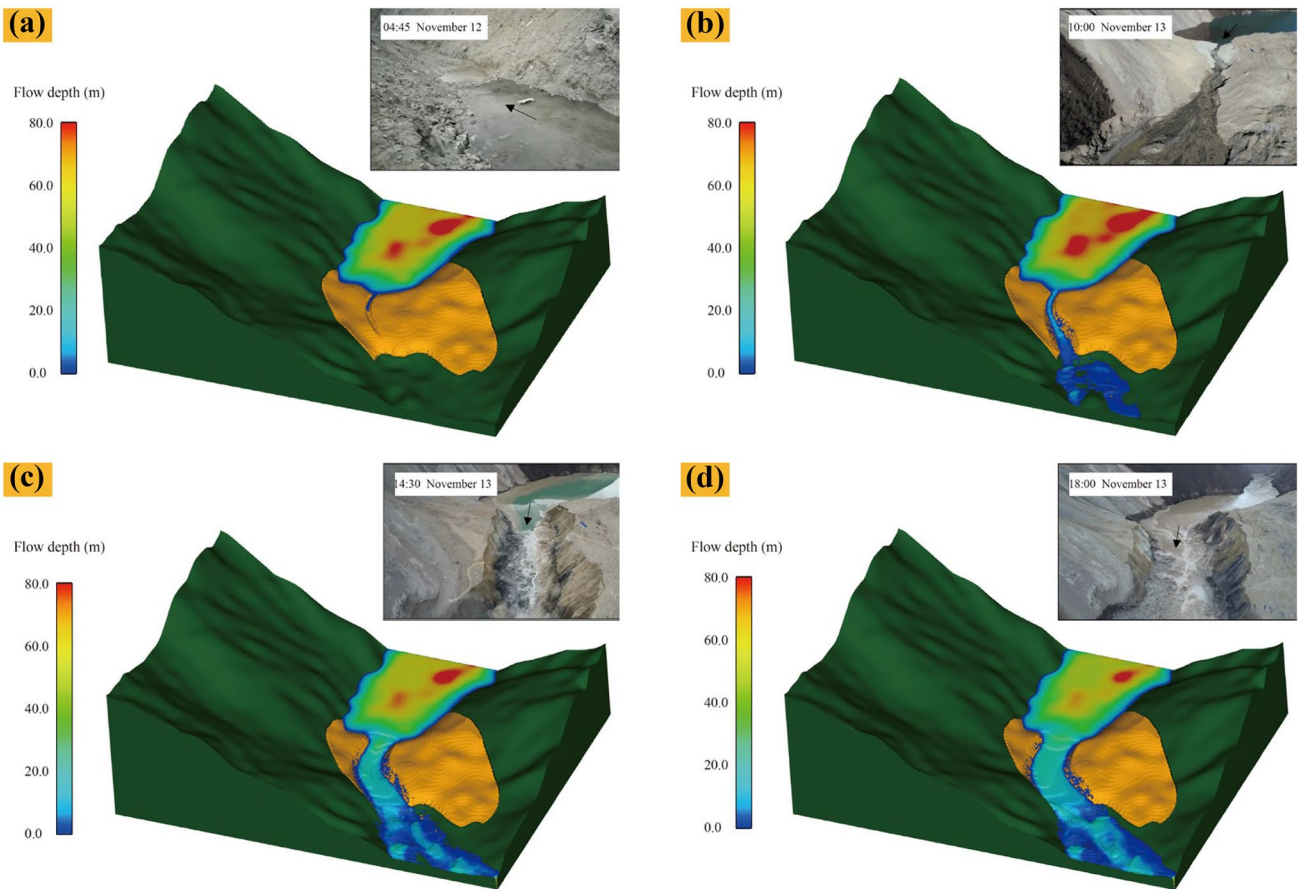


**Fig. 15** Comparison of calculated and measured dynamic breach process. **a** Overflow of the spillway (04:45, November 12); **b** backward erosion (10:00, November 13); **c** streamwise erosion (14:30, November 13); **d** rebalance of the breach channel (18:00, November 13)

can be speculated that the erosion form of the breach transitions from longitudinal undercutting to lateral expansion. In stage 3, the average flow velocity of each monitoring point was consistent, and the free surface and flow depth also tended to be the same.

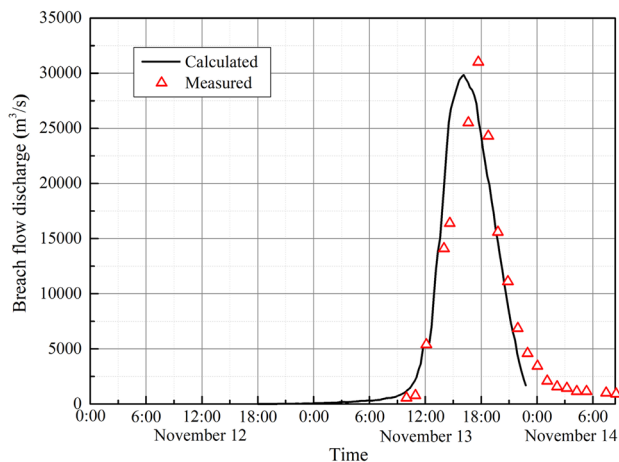


**Fig. 16** Comparison of the calculated and measured breach hydrographs

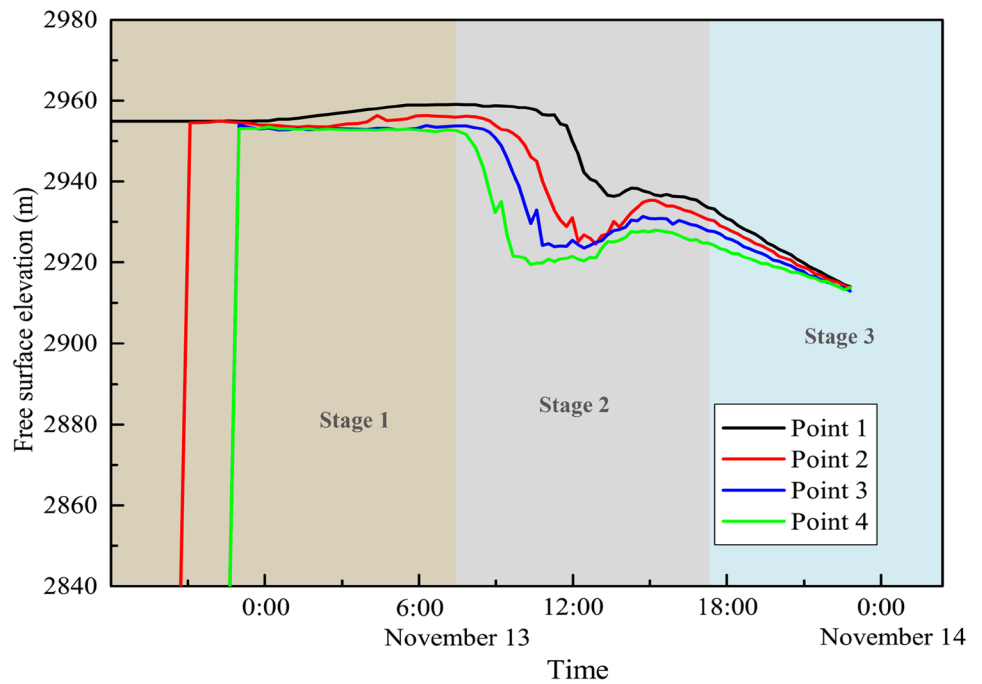
### Breach morphology

Using an unmanned aerial vehicle (UAV), a three-dimension model for the final breach morphology was reconstructed by Cai et al. (2020). Detailed cross-sections of the residual dam can be obtained by laser scanning from a UAV (Fig. 14). Accordingly, Fig. 20 presents the four typical sections of the inlet (Sect. 1-1') and turning point of the breach channel (Sect. 2-2'), the expansion area at the downstream slope (Sect. 3-3'), and the outlet (Sect. 4-4') of breach channel in the output of the numerical model, which corresponds to the measured sections (II, V, VII, and XI in Fig. 14b). The downstream slope ratio of the residual dam decreased after dam breaching, which is consistent with the description of the breach process (the incision and deposition

**Table 3** Calculated and measured breaching parameters

Parameter	$Q_p$ (m <sup>3</sup> /s)	$T_p$ (h)
Measured	31,000	37.25
Calculated	29,518	35.06
Relative error (%)	-4.78	-5.88

**Fig. 17** Variations of the free surface elevation with time at different monitoring points



effects) based on the model tests (Fig. 21). Furthermore, Fig. 22 shows the calculated and measured final breach morphologies at the four cross-sections, and the model predictions are consistent with the measured data. In contrast, there is a gap between the final breach morphology at the turning point (Sect. 2-2') of the spillway and the measured data because of the complex flow situation (Fig. 22b). Due to limitations of the steep valleys on both

sides of the breach channel, the expansion area at the downstream slope (Sect. 3-3') shows weaker lateral erosion than the other sections (Fig. 22c). In addition, the final breach elevation at the landslide dam toe (Sect. 4-4') exhibits relatively lower elevation due to the constant flooding during dam breaching (Fig. 22d). Overall, the simulation results can provide an accurate visualization of the final breach morphology.

**Fig. 18** Variations of the flow depth with time at different monitoring points

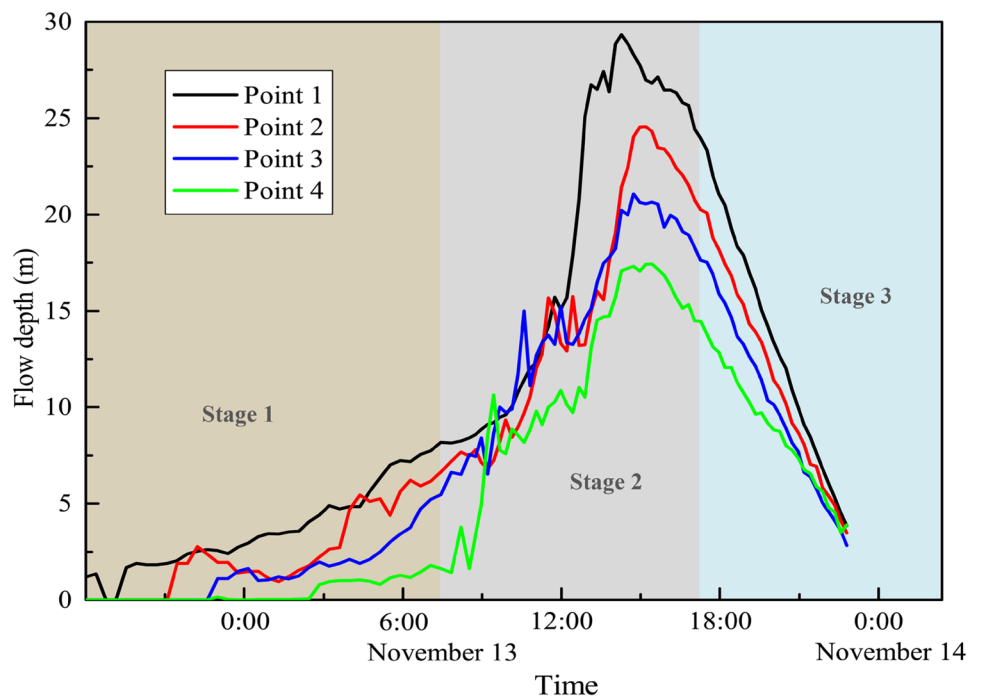
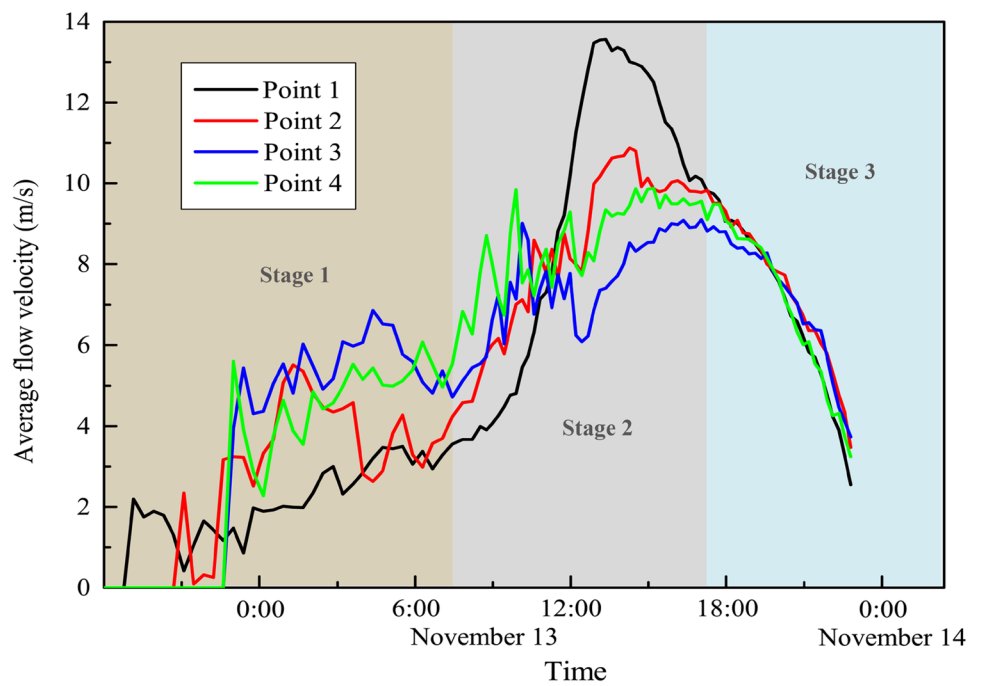




**Fig. 19** Variations of the average flow velocity with time at different monitoring points



#### Comparison with other typical breach models

The results obtained here are compared with some typical breach models to testify the numerical simulation method's rationality and applicability. It is well known that the empirical models are simple to use and usually have the same outputs from different users using

the same input parameters. Hence, five typical empirical models for landslide dam breaching, i.e., Costa (1985), Evans (1986), Costa and Schuster (1988), Walder and O'Connor (1997), and Peng and Zhang (2012), are selected to simulate the breaching parameters. Three simplified physically based models, such as DABA (Chang and Zhang 2010), DB-IWHR (Chen et al. 2015a), and DB-NHRI (Zhong

**Fig. 20** Locations of the four cross sections in the output of the numerical model

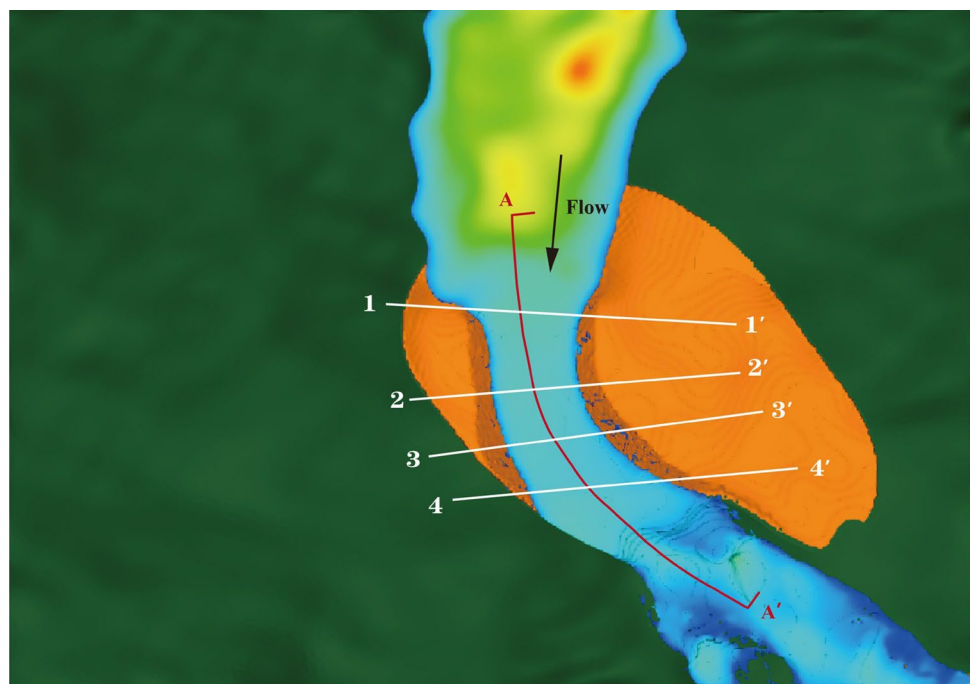
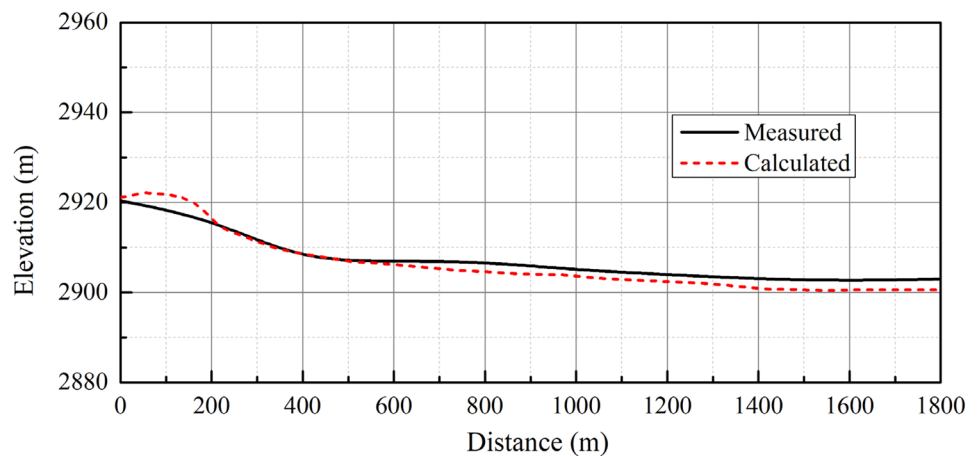


**Fig. 21** Comparison of the calculated and measured topographies in the longitudinal section after breaching



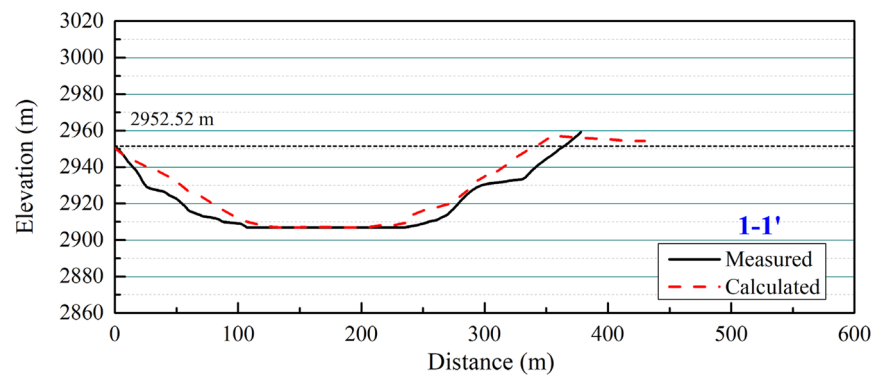
et al. 2020b), are also selected. Furthermore, a detailed physically based model, namely, 2D double layer-averaged two-phase model (Li et al. 2021), is also selected. The selection of these three simplified physically based models and one detailed physically based mode is because they have conducted the back analysis of the “11.03” Baige landslide dam breach case (Zhang et al. 2019; Cai et al. 2020; Zhong et al. 2020a; Li et al. 2021), and the calculated breaching parameters can be directly chosen for comparison based on the reported results. Because of the complexity calculated processes of the other physically based models, to be fair, only the above four physically based models are chosen for comparison in this section. A brief introduction of the empirical models and physically based models for the comparison are shown in Tables 4 and 5, respectively. The key breaching parameters such as peak breach flow ( $Q_p$ ), final breach top width ( $B_f$ ), final breach bottom width ( $b_f$ ), final breach depth ( $D_f$ ), and time to peak ( $T_p$ ) calculated by these models for the “11.03” Baige landslide dam are listed in Table 6. It is worth noted that, due to the complexity of final breach morphology, most of the empirical model do not provide the final breach size. Because the length of breach channel along the streamwise direction often has a relatively large value, the final breach top and bottom widths in Table 6 means the width of breach on the crest and at the bottom of the landslide dam, which are measured parallel to the main valley axis. The final breach depth means the vertical distance from the lowest bottom of the breach to the original lowest point on the landslide dam crest.

In Table 6, for empirical models, the calculated peak breach flows by the model of Evans (1986) and full-variable equation of the model of Peng and Zhang (2012) have the relative errors less than  $\pm 10\%$ , while the calculated peak breach flows by the other models are greater than  $\pm 25\%$ . In addition, the calculated breach size of the full-variable and simplified equations of the model of Peng and Zhang (2012) have relative errors of less than  $\pm 20$

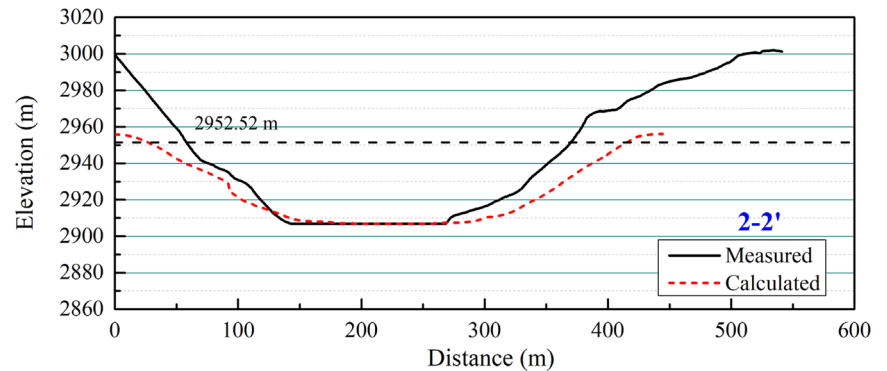
and  $\pm 30\%$ , respectively. In general, the model of Peng and Zhang (2012) adequately predicts the “11.03” Baige landslide dam breach parameters. The most critical shortcoming is that the five empirical models neglect the breach processes, and only the model of Peng and Zhang (2012) considers the soil properties of landslide deposits. In addition, only the model of Peng and Zhang (2012) can simulate the final breach size and the failure time. However, the statistical methods for dam failure time are different, and more importantly, it cannot calculate the occurrence time of peak flow discharge. Therefore, the failure time analysis of the parametric models is not carried out in this study.

Due to the high computational efficiency and acceptable errors, simplified physically based models are widely used in the emergency response for landslide dam breaching. As shown in Table 6, the three simplified physically based models can reasonably predict the peak breach flow and time to peak with relative errors less than  $\pm 10\%$ , except for the calculated peak breach flow by the model of Zhang et al. (2019), with a relative error of 10.8%. It is noted that these models can only obtain the breach size under the assumption of a regular cross-section, which usually deviates from the actual breach evolution. Concurrently, the influence of the actual 3D terrain on the breach process cannot be reflected based on the simplified section assumption. Therefore, the accuracy of the empirical and simplified physically based models depends on their physical assumptions and input parameters, which have high uncertainty. In addition, the detailed physically based model, namely the 2D double layer-averaged two-phase flow model (Li et al. 2021), presented a good performance on peak breach flow and time to peak, with relative errors less than  $\pm 10\%$ . In contrast, the numerical simulation method proposed in this study utilizes the three-dimensional Navier–Stokes equations to control the flow dynamics, providing the three-dimensional visualization information of dam failure based on time variation.

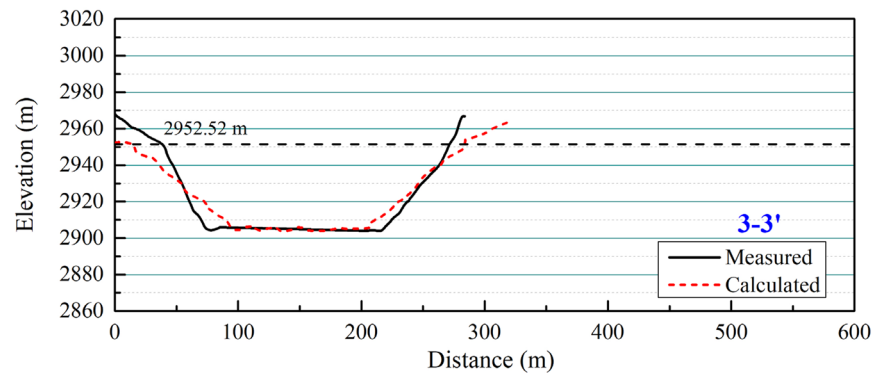
**Fig. 22** Comparison of the calculated and measured final breach topographies at the four cross sections from Fig. 20. **a** Sect. 1-1'; **b** Sect. 2-2'; **c** Sect. 3-3'; **d** Sect. 4-4'



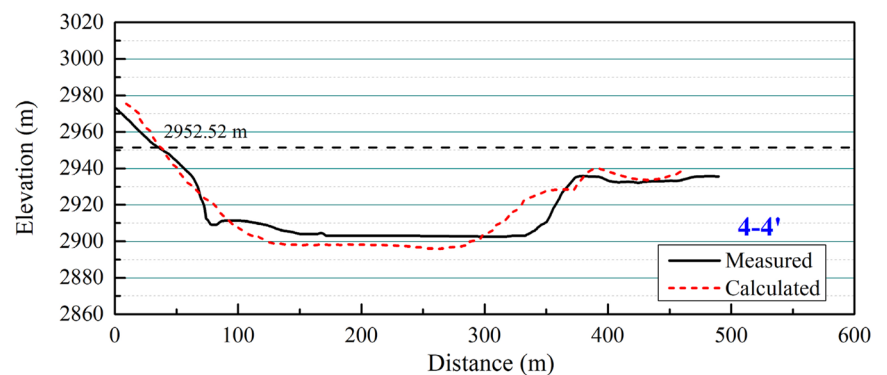
**(a)** Section 1-1'



**(b)** Section 2-2'



**(c)** Section 3-3'



**(d)** Section 4-4'

**Table 4** A brief introduction of the typical empirical models for landslide dam breaching

No.	Investigators	No. of cases	Expressions
1	Costa (1985)	10	$Q_p = 6.3H_d^{1.59} \quad (14)$ $Q_p = 672V_l^{0.56} \quad (15)$ $Q_p = 181(H_d V_l')^{0.43} \quad (16)$
2	Evans (1986)	29	$Q_p = 0.72V_l^{0.53} \quad (17)$
3	Costa and Schuster (1988)	12	$Q_p = 0.0158(PE)^{0.41} \quad (18)$
4	Walder and O'Connor (1997)	18	$Q_p = 1.6V_r^{0.46} \quad (19)$ $Q_p = 6.7d_d^{1.73} \quad (20)$ $Q_p = 0.99(d_d \cdot V_r)^{0.40} \quad (21)$
5	Peng and Zhang (2012)	45	<p>Full-variable equation: <math display="block">\frac{Q_p}{g^{\frac{1}{2}} H_d^{\frac{5}{2}}} = \left(\frac{H_d}{H_0}\right)^{-1.417} \left(\frac{H_d}{W_d}\right)^{-0.265} \left(\frac{V_d^{\frac{1}{3}}}{H_d}\right)^{-0.471} \left(\frac{V_l^{\frac{1}{3}}}{H_d}\right)^{1.569} e^{a_1} \quad (22)</math></p> <p>Simplified equation: <math display="block">\frac{Q_p}{g^{\frac{1}{2}} H_d^{\frac{5}{2}}} = \left(\frac{H_d}{H_0}\right)^{-1.371} \left(\frac{V_l^{\frac{1}{3}}}{H_d}\right)^{1.536} e^{a_2} \quad (23)</math></p>
		13	<p>Full-variable equation: <math display="block">\frac{B_f}{H_0} = \left(\frac{H_d}{H_0}\right)^{0.752} \left(\frac{H_d}{W_d}\right)^{0.315} \left(\frac{V_d^{\frac{1}{3}}}{H_d}\right)^{-0.243} \left(\frac{V_l^{\frac{1}{3}}}{H_d}\right)^{0.682} e^{a_3} \quad (24)</math></p> <p>Simplified equation: <math display="block">\frac{B_f}{H_0} = \left(\frac{H_d}{H_0}\right)^{0.911} \left(\frac{V_l^{\frac{1}{3}}}{H_d}\right)^{0.271} e^{a_4} \quad (25)</math></p>
		10	<p>Full-variable equation: <math display="block">\frac{b_f}{H_d} = 0.004\left(\frac{H_d}{H_0}\right) + 0.050\left(\frac{H_d}{W_d}\right) - 0.044\left(\frac{V_d^{\frac{1}{3}}}{H_d}\right) + 0.088\left(\frac{V_l^{\frac{1}{3}}}{H_d}\right) + a_5 \quad (26)</math></p> <p>Simplified equation: <math display="block">\frac{b_f}{H_d} = 0.003\left(\frac{H_d}{H_0}\right) + 0.070\left(\frac{V_l^{\frac{1}{3}}}{H_d}\right) + a_6 \quad (27)</math></p>
		21	<p>Full-variable equation: <math display="block">\frac{D_f}{H_0} = \left(\frac{H_d}{H_0}\right)^{0.882} \left(\frac{H_d}{W_d}\right)^{-0.041} \left(\frac{V_d^{\frac{1}{3}}}{H_d}\right)^{-0.099} \left(\frac{V_l^{\frac{1}{3}}}{H_d}\right)^{0.139} e^{a_7} \quad (28)</math></p> <p>Simplified equation: <math display="block">\frac{D_f}{H_0} = \left(\frac{H_d}{H_0}\right)^{0.923} \left(\frac{V_l^{\frac{1}{3}}}{H_d}\right)^{0.118} e^{a_8} \quad (29)</math></p>

$Q_p$ , peak breach flow with the unit of  $m^3/s$ ;  $V_d$ , landslide dam volume with the unit of  $m^3$ ;  $V_l$ , dammed lake volume with the unit of  $m^3$ ;  $V_l'$ , dammed lake volume with the unit of  $10^6 m^3$ ;  $H_d$ , landslide dam height with the unit of  $m$ ;  $H_0$ , unit height with the unit of  $m$ ;  $g$ , gravitational acceleration with the unit of  $m/s^2$ ;  $W_d$ , landslide dam width with the unit of  $m$ ;  $PE$ , potential energy with the unit of joule with the unit of  $J$ ;  $d_d$ , drop in dammed lake level with the unit of  $m$ ;  $V_r$ , released water volume of the dammed lake with the unit of  $m^3$ ;  $B_f$ , final breach top with the unit of  $m$ ;  $b_f$ , final breach bottom width with the unit of  $m$ ;  $D_f$ , final breach depth with the unit of  $m$ ;  $T_f$ , failure time with the unit of  $h$ ;  $T_o$ , unit time with the unit of  $h$ .  $a_1=1.276$  for dam material with high erodibility,  $a_1=-0.336$  for dam material with medium erodibility,  $a_1=-1.532$  for dam material with low erodibility;  $a_2=1.236$  for dam material with high erodibility,  $a_2=-0.380$  for dam material with medium erodibility,  $a_2=-1.615$  for dam material with low erodibility;  $a_3=1.683$  for dam material with high erodibility,  $a_3=1.201$  for dam material with medium erodibility,  $a_3$  is unavailable for dam material with low erodibility;  $a_4=0.588$  for dam material with high erodibility,  $a_4=0.148$  for dam material with medium erodibility,  $a_4$  is unavailable for dam material with low erodibility;  $a_5=0.775$  for dam material with high erodibility,  $a_5=0.532$  for dam material with medium erodibility,  $a_5$  is unavailable for dam material with low erodibility;  $a_6=0.624$  for dam material with high erodibility,  $a_6=0.344$  for dam material with medium erodibility,  $a_6$  is unavailable for dam material with low erodibility;  $a_7=-0.316$  for dam material with high erodibility,  $a_7=-0.520$  for dam material with medium erodibility,  $a_7$  is unavailable for dam material with low erodibility;  $a_8=-0.500$  for dam material with high erodibility,  $a_8=-0.673$  for dam material with medium erodibility,  $a_8$  is unavailable for dam material with low erodibility;  $a_9=-0.635$  for dam material with high erodibility,  $a_9=-0.518$  for dam material with medium erodibility,  $a_9$  is unavailable for dam material with low erodibility;  $a_{10}=-0.805$  for dam material with high erodibility,  $a_{10}=-0.674$  for dam material with medium erodibility,  $a_{10}$  is unavailable for dam material with low erodibility

**Table 5** A brief introduction of simplified and detailed typical physically based models for landslide dam breaching

No.	Investigators	Dam structure	Breach morphology		Breach flow discharge	Erosion characteristics	Mechanical mechanisms
			Cross section	Longitudinal section			
1	DABA (Zhang et al. 2019)	Multilayer	Breach side slope angle increased to a certain value and then remain constant	Downstream slope angle increased to a certain value and then remained constant	Broad-crested weir flow equation	Stress-based erosion rate equation considering variations in soil erodibility coefficient with depth	/
2	DB-IWHR (Cai et al. 2020)	Monolayer	Breach side slope angle remain constant until instability occurred	Remain constant downstream slope angle	Broad-crested weir flow equation	Hyperbolic erosion rate equation	Instability of breach side slopes with circular or planar slip surface
3	DB-NHRI (Zhong et al. 2020a)	Multilayer	Breach side slope angle remain constant until instability occurred	Continuous decrease of downstream slope angle	Broad-crested weir flow equation	Stress-based erosion rate equation considering variations in grain size distribution and soil erodibility coefficient with depth	Instability of breach side slopes with planar slip surface
4	2D double layer-averaged two-phase flow model (Li et al. 2021)	Multi grain sizes	Mass change with the bed and interphase and inter-grain size interaction	Mass change with the bed and interphase and inter-grain size interaction	Multiplication of the flow velocity and area	Sediment mass conservation	The effects of steep slopes on sediment transport

**Table 6** Breaching parameters from typical breach models for the “11.03” Baige landslide dam

Investigators	Comparison	$Q_p$ (m <sup>3</sup> /s)	$B_f$ (m)	$b_f$ (m)	$D_f$ (m)	$T_p$ (h)
Costa (1985)	Calculated result	8936 (Eq. (14))	—	—	—	—
	Relative error	-71.17%	—	—	—	—
	Calculated result	21,670 (Eq. (15))	—	—	—	—
	Relative error	-30.10%	—	—	—	—
	Calculated result	18,551 (Eq. (16))	—	—	—	—
	Relative error	-40.16%	—	—	—	—
	Calculated result	29,175 (Eq. (17))	—	—	—	—
	Relative error	-5.88%	—	—	—	—
Costa and Schuster (1988)	Calculated result	15,204 (Eq. (18))	—	—	—	—
	Relative error	-50.95%	—	—	—	—
Walder and O'Connor (1997)	Calculated result	15,967 (Eq. (19))	—	—	—	—
	Relative error	-48.49%	—	—	—	—
	Calculated result	13,420 (Eq. (20))	—	—	—	—
	Relative error	-56.71%	—	—	—	—
	Calculated result	17,239 (Eq. (21))	—	—	—	—
	Relative error	-44.39%	—	—	—	—
	Calculated result	28,267 (Eq. (22))	228.04 (Eq. (24))	126.08 (Eq. (26))	57.32 (Eq. (28))	—
	Relative error	-8.82%	-13.65%	16.96%	-7.54%	—
Peng and Zhang (2012)	Calculated result	22,695 (Eq. (23))	186.69 (Eq. (25))	130.98 (Eq. (27))	52.55 (Eq. (29))	—
	Relative error	-26.79%	-29.31%	21.51%	-15.25%	—
Zhang et al. (2019)	Calculated result	34,348	337.4	139.8	70.5	37.9
	Relative error	10.8%	27.75%	29.68%	13.71%	1.74%
Cai et al. (2020)	Calculated result	31,041	—	—	—	37.83
	Relative error	0.13%	—	—	—	1.56%
Zhong et al. (2020a)	Calculated result	28,613.1	261.8	100.3	70.2	37.47
	Relative error	-7.7%	-0.9%	-7.0%	13.2%	0.6%
Li et al. (2021)	Calculated result	32,787	—	—	—	36.5
	Relative error	5.76%	—	—	—	-2.01%
The new model	Calculated result	29,518	—	—	—	35.06
	Relative error	-4.78%	—	—	—	-5.88%

## Conclusions

The enormous floods caused by a landslide dam breach can bring catastrophic consequences. In this study, a detailed physically based model was proposed for numerical modeling of landslide dam breaching. The following conclusions can be drawn:

(1) The detailed physically based three-dimensional model developed for landslide dam breaching can describe the hydrodynamic features of the dam-break flow, especially for turbulent flow. By comparing several representative bedload formulas, it is concluded that the Meyer-Peter and Muller formula has the best performance in different sediment transport stages when considering the broad graded characteristics of landslide dam deposits. Furthermore, the evolution process of the breach bed elevation can be accurately obtained by the equilibrium sedi-

ment transport formula combining bed load and suspended load. Finally, the slope stability can be determined by calculating the slope angle formed by the bed elevation of the center grid and the adjacent grids, which effectively ensures the simulation quality of the breach morphology evolution.

(2) The newly developed model has been verified by a benchmark experiment case of dam-break flows over mobile beds. Considering the complexity of the three-dimensional dam-break flow and the challenges brought by fluid dynamics, the calculated water level, and bed elevation results are generally in good agreement with the experimentally measured data.

(3) Rapid spatial information processing technology was utilized to reconstruct the three-dimensional topography-based model for the “11.03” Baige landslide dam. The model performance has good accordance between the measured data and numerical simulation results on breach hydrograph and breach morphol-

ogy. The relative errors on peak breach flow and time to the peak were both less than  $\pm 10\%$ . Furthermore, the simulated dynamic breach process was generally consistent with the video records, and the analyses verified the three development stages of landslide dam breaching. Monitoring points set at key positions gave the physical parameters, providing a reference for analyzing the breach process. Also, four typical final breach sections were selected on the residual dam body. The final morphologies of the calculated cross-sections were consistent with the measured data.

(4) Five empirical models, three simplified physically based models, and one detailed physically based model for the numerical simulation of landslide dam breaching were compared with the newly developed numerical model. Comparing the breaching parameters of the “11.03” Baige landslide dam failure case indicated that the newly developed simulation method performs well when calculating the breach hydrograph, especially the three-dimensional breach morphology evolution process during the landslide dam breaching. The present numerical model not only solves the problem that the empirical models cannot obtain the breach hydrograph and breach morphology evolution process, but also overcomes the defect that the simplified physically based models pre-assume the geometric shape of the breach. In addition, the present work can accurately reflect the breach process of landslide dams under complex three-dimensional terrain, while the current detailed physically based model can merely show the two-dimensional breach process.

(5) The numerical modeling in this study can contribute to understanding landslide dam breach mechanisms and provide helpful guidance for emergency disposal. Inevitably, due to the incomplete understanding of sediment transport of wide graded landslide deposits, further studies and independent tests are needed to validate, improve, and compare to the newly developed numerical simulation method.

### Acknowledgements

This work has been financially supported by the National Natural Science Foundation of China (grant nos. U2040221 and 51779153), the National Key Research and Development Program of China (grant no. 2018YFC1508604), and the Fundamental Research Funds for Central Public Research Institutes (grant no. Y320005).

### Data availability

All data used in this study are available from the corresponding author upon request.

### Declarations

**Competing interests** The authors declare no competing interests.

### References

ASCE/EWRI Task Committee on Dam/Levee Breach (2011) Earthen embankment breaching. *J Hydraul Eng* 137(12):1549–1564

Bagnold RA (1966) An approach to the sediment transport problem from general physics. U.S. Geological Survey Professional Paper 422(1):231–291

Cai YJ, Cheng HY, Wu SF, Yang QG, Wang L, Luan YS, Chen ZY (2020) Breaches of the Baige barrier lake: emergency response and dam breach flood. *SCIENCE CHINA Technol Sci* 63(7):1164–1176

Chang DS, Zhang LM (2010) Simulation of the erosion process of landslide dams due to overtopping considering variations in soil erodibility along depth. *Natural Hazards and Earth System Science* 10(4):933–946

Chen C, Zhang LM, Xiao T, He J (2020a) Barrier lake bursting and flood routing in the Yarlung Tsangpo Grand Canyon in October 2018. *J Hydrol* 583:124603

Chen SC, Lin TW, Chen CY (2015a) Modeling of natural dam failure modes and downstream riverbed morphological changes with different dam materials in a flume test. *Eng Geol* 188:148–158

Chen SJ, Chen ZY, Tao R, Yu S, Xu WJ, Zhou XB, Zhou ZD (2018) Emergency response and back analysis of the failures of earthquake triggered cascade landslide dams on the Mianyuan River. *China Natural Hazards Review* 19(3):05018005

Chen ZY, Ma LQ, Yu S, Chen SJ, Zhou XB, Sun P, Li X (2015b) Back analysis of the draining process of the Tangjiashan barrier lake. *J Hydraul Eng* 141(4):05014011

Chen ZY, Zhang Q, Chen SJ, Wang L, Zhou XB (2020b) Evaluation of barrier lake breach floods - insights from recent case studies in China. *Wires Water* 7(2):e1408

Chien N, Wan ZH (1983) *Mechanics of sediment movement*. Science Press, Beijing, China (in Chinese)

Chien N, Wan ZH (1999) *Mechanics of sediment transport*. ASCE Press, Reston, USA

Costa JE, Schuster RL (1988) The formation and failure of natural dam. *Geol Soc Am Bull* 100:1054–1068

Costa JE (1985) *Floods from dam failures*. U.S. Geological Survey, Open-File Report 85–560, Washington DC, USA

Cui P, Zhu YY, Han YS, Chen XQ, Zhuang JQ (2009) The May 12 Wenchuan earthquake-induced landslide-dammed lakes: distribution and preliminary risk evaluation. *Landslides* 7(6):209–223

Cui P, Zhou GGD, Zhu XH, Zhang JQ (2013) Scale amplification of natural debris flows caused by cascading landslide dam failures. *Geomorphology* 182:173–189

Duan HZ, Shen JN, Li YP (2012) Comparative analysis of HPDC process of an auto part with ProCAST and FLOW-3D. *Appl Mech Mater* 184:90–94

Engelund F, Fredsoe J (1976) A sediment transport model for straight alluvial channels. *Nord Hydrol* 7(5):293–306

Evans SG (1986) The maximum discharge of outburst floods caused by the breaching of man-made and natural dams. *Can Geotech J* 23(3):385–387

Fan XM, Dufresne A, Subramanian SS, Strom A, Hermanns R, Stefanelli CT, Hewitt K, Yunus AP, Dunning S, Capra L, Geertsema M, Miller B, Casagli N, Jansen JD, Xu Q (2020) The formation and impact on landslide dams - state of the art. *Earth Sci Rev* 203:103116

Fan XM, Xu Q, Alonso-Rodriguez A, Subramanian SS, Li WL, Zheng G, Dong XJ, Huang RQ (2019) Successive landsliding and damming of the Jinsha River in eastern Tibet, China: prime investigation, early warning, and emergency response. *Landslides* 16(5):1003–1020

Fourtakas G, Rogers BD (2016) Modelling multi-phase liquid-sediment scour and resuspension induced by rapid flows using smoothed particle hydrodynamics (SPH) accelerated with a graphics processing unit (GPU). *Adv Water Resour* 92:186–199

Gregoretti C, Maltauro A, Lanzoni S (2010) Laboratory experiments on the failure of coarse homogeneous sediment natural dams on a sloping bed. *J Hydraul Eng* 136(11):868–879

Guan MF, Wright NG, Sleigh PA (2014) 2D process-based morphodynamic model for flooding by noncohesive dyke breach. *J Hydraul Eng* 140(7):04014022

He ZG, Wu T, Weng HX, Hu P, Wu GF (2017) Numerical simulation of dam-break flow and bed change considering the vegetation effects. *Int J Sedim Res* 32:105–120

Hirt CW, Nichols BD (1981) Volume of fluid (VOF) method for the dynamics of free boundaries. *J Comput Phys* 39(1):201–225

International Association for Hydraulic Research (IAHR) Working Group for Dam-Break Flows over Mobile Beds (2012) *Dam-break flows over mobile beds: experiments and benchmark tests for numerical models*. *J Hydraul Res* 50(4):364–375

- Issakhov A, Imanberdiyeva M (2019) Numerical simulation of the movement of water surface of dam break flow by VOF methods for various obstacles. *International Journal of Heat and Mass Transfer* 136:1030–1051
- Issakhov A, Zhandaulet Y (2020) Numerical study of dam break waves on movable beds for complex terrain by volume of fluid method. *Water Resour Manage* 34(2):463–480
- Jiang XG, Wu L (2020) Influence of initial soil moisture on breaching mechanism of natural dam. *Journal of Jilin University (earth Science Edition)* 50(1):185–193 (in Chinese)
- Jiang XG, Wei YW (2020) Erosion characteristics of outburst floods on channel beds under the conditions of different natural dam downstream slope angles. *Landslides* 17(4):1823–1834
- Kaurav R, Mohapatra P (2019) Studying the peak discharge through a planar dam breach. *J Hydraul Eng* 145(6):06019010
- Li J, Cao ZX, Cui YF, Fan XM, Yang WJ, Huang W, Borthwick A (2021) Hydro-sediment-morphodynamic processes of the Baige landslide-induced barrier lake, Jinsha River. *China Journal of Hydrology* 596:126134
- Liang CF, Abbasi S, Pourshahbaz H, Taghvaei P, Tfwala S (2019) Investigation of flow, erosion, and sedimentation pattern around varied groynes under different hydraulic and geometric conditions: a numerical study. *Water* 11(2):235
- Liu N, Chen ZY, Zhang JX, Lin W, Chen WY, Xu WJ (2010) Draining the Tangjiashan barrier lake. *J Hydraul Eng* 136(11):914–923
- Marsooli R, Wu WM (2015) Three-dimensional numerical modelling of dam-break flows with sediment transport over movable beds. *J Hydraul Eng* 141(1):04014066
- Mastbergen DR, Berg J (2010) Breaching in fine sands and the generation of sustained turbidity currents in submarine canyons. *Sedimentology* 50(4):625–637
- Mei SY, Chen SS, Zhong QM, Shan YB (2021) Effects of grain size distribution on landslide dam breaching-insights from recent cases in China. *Front Earth Sci* 9:658578
- Meyer-Peter E, Muller R (1948) Formulas for bedload transport. *Process of Congress IAHR* 6(2):39–64
- Movahedi A, Kavianpour MR, Yamini OA (2018) Evaluation and modeling scouring and sedimentation around downstream of large dams. *Environmental Earth Sciences* 77(8):320
- Nielsen P (1992) Coastal bottom boundary layers and sediment transport. *Advanced Series on Ocean Engineering, Volume 4*, World Scientific, Singapore
- Peng M, Zhang LM (2012) Breaching parameters of landslide dams. *Landslides* 9(1):13–31
- Peng M, Ma CY, Chen HX, Zhang P, Zhang LM, Jiang MZ, Zhang QZ, Shi ZM (2021) Experimental study on breaching mechanisms of landslide dams composed of different materials under surge waves. *Eng Geol* 291:106242
- Peng M, Zhang LM, Chang DS, Shi ZM (2014) Engineering risk mitigation measures for the landslide dams induced by the 2008 Wenchuan earthquake. *Eng Geol* 180:68–84
- Roseberry JC, Schmeeckle MW, Furbish DJ (2012) A probabilistic description of the bed load sediment flux: 2. Particle activity and motions. *J Geophys Res Earth Surf* 117:F03032
- Rowan T, Seaid M (2020) Two-dimensional numerical modelling of shallow water flows over multilayer movable beds. *Appl Math Model* 88:474–497
- Samma H, Khosrojerdi A, Rostam-Abadi M, Mehraein M, Catao-Lopera Y (2020) Numerical simulation of scour and flow field over movable bed induced by a submerged wall jet. *J Hydroinf* 22(2):385–401
- Shan YB, Chen SS, Zhong QM, Mei SY, Yang M (2022) Development of an empirical model for predicting peak breach flow of landslide dams. *Landslides*. <https://doi.org/10.1007/s10346-022-01863-1>
- Shen DY, Shi ZM, Peng M, Zhang LM, Jiang MZ (2020a) Longevity analysis of landslide dams. *Landslides* 17(8):1797–1821
- Shen GZ, Sheng JB, Xiang Y, Zhong QM, Yang DW (2020b) Numerical modeling of overtopping-induced breach of landslide dams. *Nat Hazard Rev* 21(2):04020002
- Shi ZM, Guan SG, Peng M, Zhang LM, Zhu Y, Cai QP (2015) Cascading breaching of the Tangjiashan landslide dam and two smaller downstream landslide dams. *Eng Geol* 193:445–458
- Soares-Frazao S, Canelas R, Cao ZX, Cea L, Chaudhry HM, Moran AD (2012) Dam-break flows over mobile beds: experiments and benchmark tests for numerical models. *J Hydraul Res* 50(4):364–375
- Soulsby R (1997) Chapter 9: bedload transport. Thomas Telford Publications, London, Dynamics of marine sand
- Takayama S, Miyata S, Fujimoto M, Satofuka Y (2021) Numerical simulation method for predicting a flood hydrograph due to progressive failure of a landslide dam. *Landslides* 18:3655–3670
- Van Rijn L (1984) Sediment transport, part I: bed load transport. *J Hydraul Eng* 110(10):1431–1456
- Walder JS, Iverson RM, Godt JW, Logan M, Solovitz SA (2015) Controls on the breach geometry and flood hydrograph during overtopping of noncohesive earthen dams. *Water Resour Res* 51(8):6701–6724
- Walder JS, O'Connor JE (1997) Methods for predicting peak discharge of floods caused by failure of natural and constructed earthen dams. *Water Resour Res* 33(10):2337–2348
- Wang L, Chen ZY, Wang NX, Sun P, Yu S, Li SY, Du XH (2016) Modeling lateral enlargement in dam breaches using slope stability analysis based on circular slip mode. *Eng Geol* 209:70–81
- Wu WM (2013) Simplified physically based model of earthen embankment breaching. *J Hydraul Eng* 139(8):837–851
- Yakhot V, Orszag SA, Thangam S, Gatski TB, Speziale CG (1992) Development of turbulence models for shear flows by a double expansion technique. *Phys Fluids A* 4(7):1510–1520
- Yang M, Zhong QM, Shan YB, Mei SY (2021) Influences of spillway section morphologies on landslide dam breaching. *Front Earth Sci* 9:799742
- Zhao TL, Chen SS, Fu CJ, Zhong QM (2018) Influence of diversion channel section type on landslide dam draining effect. *Environ Earth Sci* 77(2):54–62
- Zhao TL, Chen SS, Fu CJ, Zhong QM (2019) Centrifugal model test on the failure mechanism of barrier dam overtopping. *KSCE J Civ Eng* 23(4):1548–1559
- Zhang JY, Fan G, Li HB, Zhou JW, Yang XG (2021) Large-scale field model tests of landslide dam breaching. *Eng Geol* 293:106322
- Zhang LM, Peng M, Chang DS, Xu Y (2016) Dam failure mechanisms and risk assessment. John Wiley & Sons Singapore Pte. Ltd., Singapore
- Zhang LM, Xiao T, He J, Chen C (2019) Erosion-based analysis of breaching of Baige landslide dams on the Jinsha River, China, in 2018. *Landslides* 16(10):1965–1979
- Zhong QM, Wang L, Chen SS, Chen ZY, Shan YB, Zhang Q, Ren Q, Mei SY, Jiang JD, Hu L, Liu JX (2021) Breaches of embankment and landslide dams - state of the art review. *Earth Sci Rev* 216:103597
- Zhong QM, Chen SS, Wang L, Shan YB (2020a) Back analysis of breaching process of Baige landslide dam. *Landslides* 17(7):1681–1692
- Zhong QM, Wu WM, Chen SS, Wang M (2016) Comparison of simplified physically based dam breach models. *Nat Hazards* 84(2):1385–1418
- Zhong QM, Chen SS, Mei SA, Cao W (2018) Numerical simulation of landslide dam breaching due to overtopping. *Landslides* 16(6):1183–1192
- Zhong QM, Chen SS, Shan YB (2020b) Prediction of the overtopping-induced breach process of the landslide dam. *Eng Geol* 274:105709
- Zhou GGD, Zhou MJ, Shrestha MS, Song DR, Choi CE, Cui KFE, Peng M, Shi ZM, Zhu XH, Chen HY (2019) Experimental investigation on the longitudinal evolution of landslide dam breaching and outburst floods. *Geomorphology* 334:29–43
- Zhou JW, Cui P, Hao MH (2016) Comprehensive analyses of the initiation and entrainment processes of the 2000 Yigong catastrophic landslide in Tibet. *China Landslides* 13(1):39–54
- Zhu XH, Liu BX, Peng JB, Zhang ZF, Zhuang JQ, Huang WL, Leng YQ, Duan Z (2021) Experimental study on the longitudinal evolution of the overtopping breaching of noncohesive landslide dams. *Eng Geol* 288:106137
- Zhu XH, Peng JB, Liu BX, Jiang C, Guo J (2020) Influence of textural properties on the failure mode and process of landslide dams. *Eng Geol* 271:105613



---

Springer Nature or its licensor holds exclusive rights to this article under a publishing agreement with the author(s) or other rightsholder(s); author self-archiving of the accepted manuscript version of this article is solely governed by the terms of such publishing agreement and applicable law.

---

**Shengyao Mei · Shengshui Chen · Qiming Zhong** (✉) ·  
**Yibo Shan**

Department of Geotechnical Engineering, Nanjing Hydraulic  
Research Institute, Nanjing 210024, China  
Email: qmzhong@nhri.cn

**Shengyao Mei · Yibo Shan**

College of Civil and Transportation Engineering, Hohai University,  
Nanjing 210098, China

**Shengyao Mei**

Email: symei@nhri.cn

**Yibo Shan**

Email: ybshan@nhri.cn

**Shengshui Chen · Qiming Zhong**

Key Laboratory of Reservoir and Dam Safety of the Ministry of Water  
Resources, Nanjing 210029, China

**Shengshui Chen**

Email: sschen@nhri.cn